In presenting this dissertation in partial fulfillment of the requirements for an advanced degree at Idaho State University, I agree that the Library shall make it freely available for inspection. I further state that permission for extensive copying of my dissertation for scholarly purposes may be granted by the Dean of the Graduate School, Dean of my academic division, or by the University Librarian. It is understood that any copying or publication of this dissertation for financial gain shall not be allowed without my written permission.

Signature ____

Date ____

POSITRON PRODUCTION EFFICIENCY STUDY USING HIGH REPETITION RATE LINAC AT IAC

by

Sadiq Setiniyaz
(Shadike Saitiniyazi)

A dissertation

submitted in partial fulfillment

of the requirements for the degree of

Doctor of Philosophy in the Department of Physics

Idaho State University

Jul 2013

To the Graduate Faculty:

The members of the committee appointed to examine the dissertation of Sadiq Setiniyaz (Shadike Saitiniyazi) find it satisfactory and recommend that it be accepted.

Tony Forest, Ph.D.
Major Advisor

Yujong Kim, Ph.D.
Committee Member

Dustin McNulty, Ph.D.
Committee Member

Mahbub A. Khandaker, Ph.D.
Committee Member

Wenxiang Zhu, Ph.D.
Committee Member

Acknowledgments

Thanks to my advisor Dr. Forest, who made this whole work possible. He always help me to the very details of my work patiently.

Thanks to Dr. Kim. He helped and directed me a lot on accelerator physics area of my research and experiments.

Thanks to Dr. Chouffani and Dr. Freyberger for their advise and direction in the experiments.

Thanks to engineers at IAC, especially Chad, Kevin, Brian.

Thanks to my friends Oleksiy, Jason, Mayir, Carlos, Zaijing, Olga, and Misha always there when I needed them, like lifting heavy stuff, lead bricks.

Also Thanks to my friends Chris, Jack, Tony, and many others.

Contents

Page

Chapter

List of Figures

List of Tables

Abstract

I propose to measure the positron production efficiency for a positron source that uses a quadrupole triplet system to collect positrons from a tungsten target that are produced when the target is impinged by electrons from the High Repetition Rate Linac (HRRL) at Idaho State University's (ISU) Idaho Accelerator Center (IAC). Positrons were observed in May of 2008 at the IAC without the use of a quadrupole triplet collection system. When a 10 MeV electron beam is used on the tungsten target, positrons escaping from the downstream side of the tungsten have a wide momentum spread of 0 to 2 MeV and a large divergence of π rad. A quad triplet collection system, after the tungsten target, is used to focus the positron beam and as a result increase our positron collection efficiency. I will install the collection system and associated beam line components and measure the positron production efficiency using the HRRL.

= Text = ==Introduction==

Chapter 1

Introduction

1.1 Positron Beam

Positrons are used in several discipline of sciences, like chemistry, physics, material science, surface science, biology and nanoscience [1]. Different approaches are used to generate positrons. The main challenge is increasing the intensity (or current) of the positron beam. One of the most common methods used to generate a positron beam is an electron linac. The electron beam produces a positron beam by bremsstrahlung and pair production. One of the advantages of the linac based positrons is its variable energy and intensity.

Positron annihilation spectroscopy is a non-damaging technique to detect defects in materials. It is based on the fact that positrons tend to annihilate near defects in the material [2]. Different depth of the materials can be probed by using variable energy positron source. A variable energy positron source may be uased to probe for defects at different material depths.

1.2 Positron Production Using Low Energy Electron Linac

The nucleon electromagnetic form factors are fundamental quantities that are related to the charge and magnetization distribution in the nucleon. Conventionally, the nucleon form factors are measured using the Rosenbluth Technique (RT) [3]. The form factor scaling ratio, $R = \mu_p G_{Ep}/G_{Mp}$, measured using this technique is around unity as shown in the figure

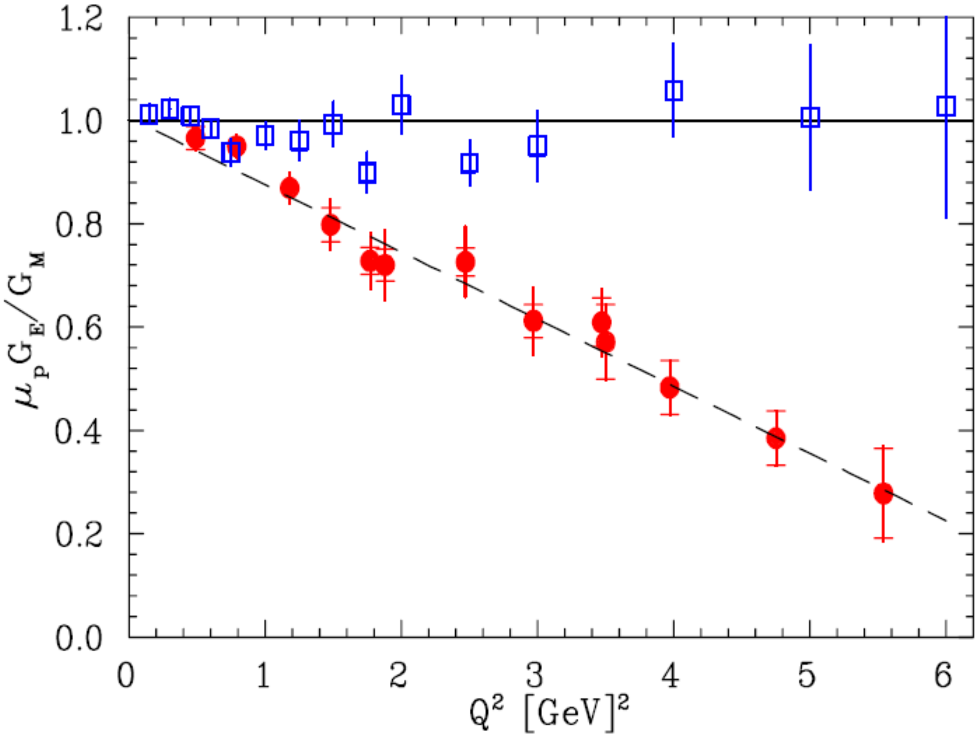

Figure 1.1: Form factor ratio, obtained by Rosenbluth Technique (hollow square) and results from Recoil Polarization Technique [5].

below [4]. Since the 1990's, a technique using elastic electron-proton polarization transfer to measurement this ratio have been developed [4–6]. In this technique, form factor scaling ratio linearly decreases as the Q^2 increases, as shown in the Fig. 1.1.

The disagreement could arise from the fact the Rosenbluth Techqniue assumes that One Photon Exchange (OPE) during the scattering while the twophoton exchange (TPE), which depends weakly on Q^2, could also become considerable with increasing Q^2 [5]. The contribution of TPE can be obtained by comparing the ratio of e^+ p to e^- p ratio. The interference of OPE and TPE can also be studied in the process $e^+e^- \to p\bar{p}$

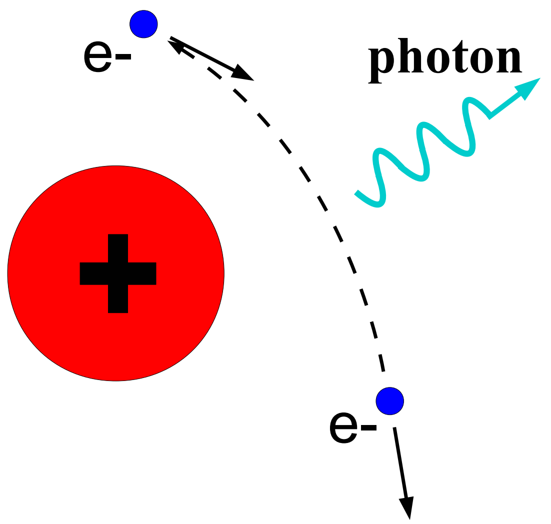

Figure 1.2: Photon generation from Bremsstrahlung processes.

1.3 Positron Beam Generation from Bremsstrahlung

When a moving charged particle interacts with the electric field of another charged particle, it can be deflected and lose energy in the form of photons, as shown in Fig. 1.2. This interaction is known as the Bremsstrahlung process. The probability of this interaction increases with the atomic number of the material traversed by the incident charged particle. Fig. 1.3 shows the photon energy distribution produced when the 12 MeV electron energy distribution from Fig. 1.4 interacts with a 1 mm thick Tungsten target. The number of photons produced decreases as the energy of the produced photon increases.

The Bremsstrahlung cross section given by Eq. 1.1 [7],

$$d\sigma = 4Z^2 r_e^2 \alpha \frac{d\nu}{\nu} \left\{ \left(1 + \left(\frac{E}{E_0} \right)^2 \right) \left[\frac{\phi_1(\gamma)}{4} - \frac{1}{3} \ln Z - f(Z) \right] - \frac{2E}{3E_0} \left[\frac{\phi_2(\gamma)}{4} - \frac{1}{3} \ln Z - f(Z) \right] \right\} \tag{1.1}$$

where, E_0 is initial total energy of the electron, E is final total energy of the electron,

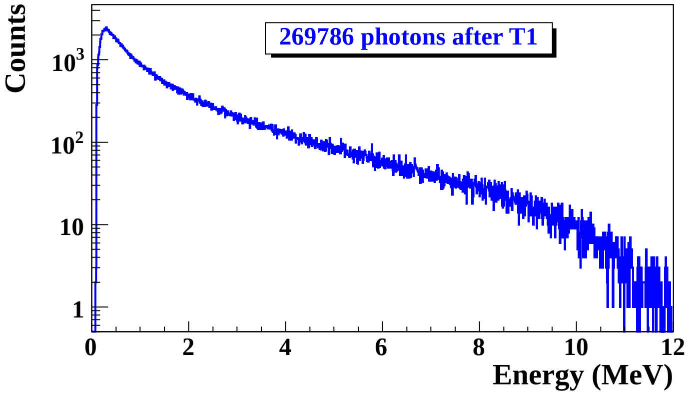

Figure 1.3: Simulated Bremsstrahlung photon energy right after a tungsten foil.

$\nu = \frac{E_0 - E}{h}$ is energy of the emitted photon, and Z is atomic number. $\gamma = \frac{100 m_e c^2 h\nu}{E_0 E Z^{1/3}}$ is charge screening parameter and $f(Z)$ is given by,

$$f(Z) = (Z\alpha)^2 \sum_{1}^{\infty} \frac{1}{n[n^2 + (Z\alpha)^2]} \tag{1.2}$$

where $\alpha = \frac{1}{137}$ is fine-structure constant, ϕ_1 and ϕ_2 are screening functions that depend on Z

There are three competing processes that a photon can undergo when interacting with matter. At electron volt (eV) energies comparable to the electron atomic binding energy, the dominant photon interaction is via the photoelectric effect. As the photon energy increases up to kilo electron volt (keV) range, the Compton scattering process starts to be more dominant. Although the photon is totally absorbed during the photoelectric effect, photons merely lose energy when undergoing Compton scattering. As the photon energy reaches twice the rest mass energy of electron, 2 × 511 keV, pair production begins to occur. Pair production becomes the dominant interaction process when photon energies are beyond 5 MeV [8]. In this process, a photon interacts with the electric field of the nucleus or the bound electrons and is converted into an electron and positron pair.

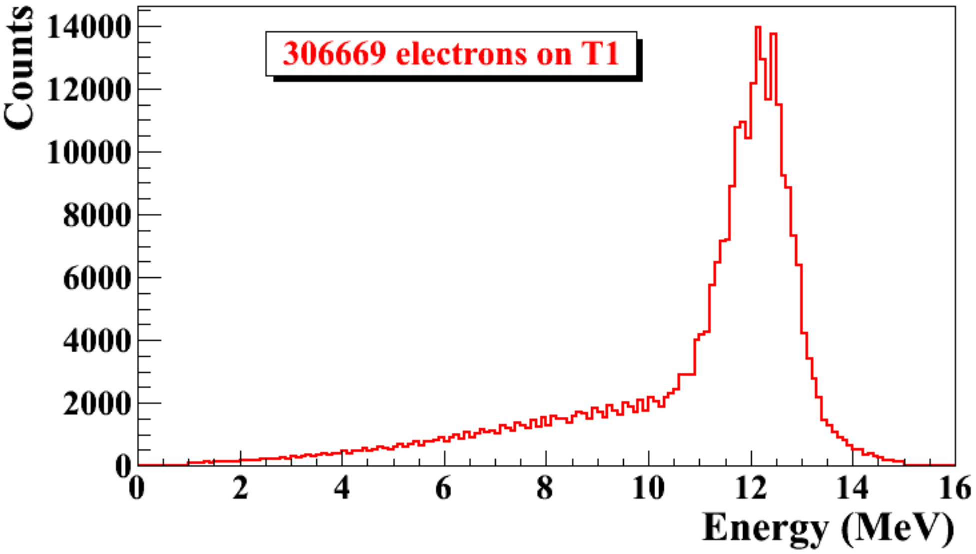

Figure 1.4: Simulated electron energy distribution right before a tungsten foil.

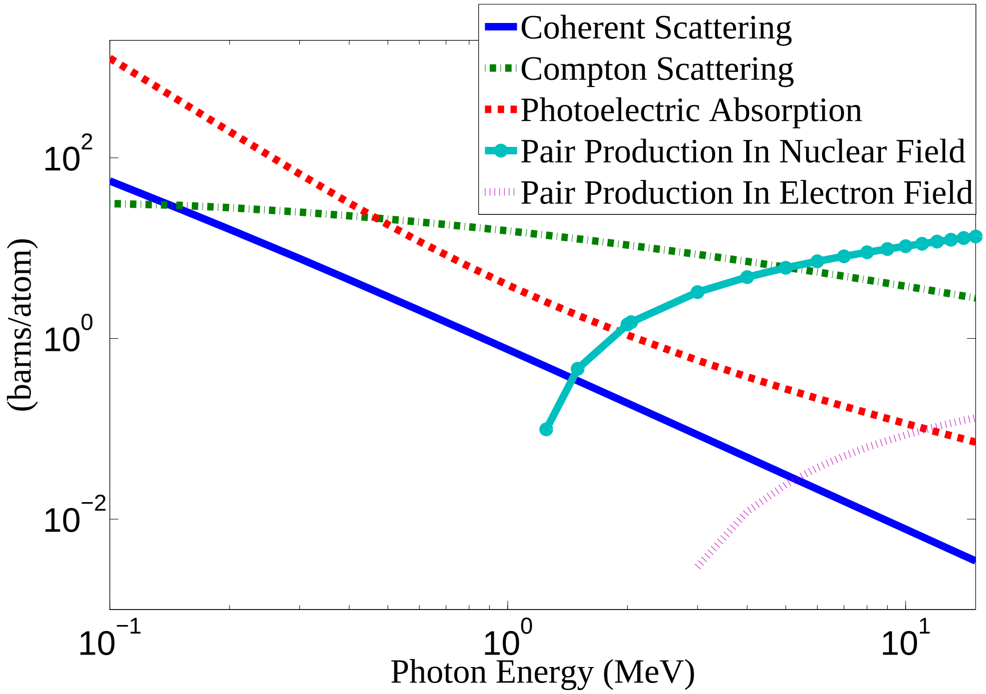

Figure 1.5: Cross section for each type of photon interaction with tungsten as function of photon energy [9].

Using natural unit, where $c \equiv 1$, the differential cross-section for pair production can be expressed as,

$$\frac{d\sigma}{d\epsilon_1 d\theta_1 d\theta_2} = 8\left(\frac{\pi a}{\sinh(\pi a)}\right)^2 \frac{a^2}{2\pi}\frac{e^2}{\hbar c}\left(\frac{\hbar}{m_e c}\right)^2 \frac{\epsilon_1\epsilon_2}{k^3}\theta_1\theta_2 \tag{1.3}$$

$$\times \Big\{ \tfrac{V^2(x)}{q^4}\left[k^2(u^2+v^2)\xi\eta - 2\epsilon_1\epsilon_2(u^2\xi^2+v^2\eta^2) + 2(\epsilon_1^2+\epsilon_2^2)uv\xi\eta cos(\phi)\right]$$

$$+a^2W^2(x)\xi^2\eta^2\left[k^2(1-(u^2+v^2)\xi\eta - 2\epsilon_1\epsilon_2(u^2\xi^2+v^2\eta^2) - 2(\epsilon_1^2+\epsilon_2^2)uv\xi\eta\cos(\phi)\right]\Big\} \tag{1.4}$$

where k is photon energy, θ_1 and θ_2 are the scattering angle of e^+ and e^- respectively, $\phi = \phi_1 - \phi_2$ is the angle between the e^+ and e^- pair, ϵ_1 and ϵ_2 are the energy of the positron and electron respectively. Other constants are $u = \epsilon_1\theta_1$, $v = \epsilon_2\theta_2$, $\xi = \frac{1}{1+u^2}$, $\eta = \frac{1}{1+v^2}$, $q^2 = u^2 + v^2 + 2uv\cos(\phi)$, $x = 1 - q^2\xi\eta$, $a = \frac{Ze^2}{\hbar c}$, and $V(x) = 1 + \frac{a^2}{(1!)^2} + \frac{a^2(1+a^2)x^2}{(2!)^2} + \frac{a^2(1+a^2)(2^2+a^2)x^4x^2}{(3!)^2} + \cdots$, $W(x) = \frac{1}{a^2}\frac{dV(x)}{dx}$.

In pair production, positron and electron pairs are created back to back in the center of mass frame. In the lab frame, electrons and positrons tend to move in the direction of photon, as shown in the Fig. 1.6. The positron and electron carry away the energy from the photon that is in excess of 1.022 MeV. In the center of mass frame, the kinetic energy is equally shared. Photons with an energy above 1.022 MeV in the bremsstrahlung spectrum of Fig.1.3 have the potential to create electron and positron pairs. The Fig. 1.7 simulation of 12 MeV mono energy 10 million electrons impinge on a tungsten target with 1.016 mm thickness. Turning on annihilation process resulted in a 511 keV peak on top of the bremsstrahlung spectrum. This 511 keV peak represents photon produced when the created positrons, from pair production, annihilates with an atomic electrons inside the tungsten target.

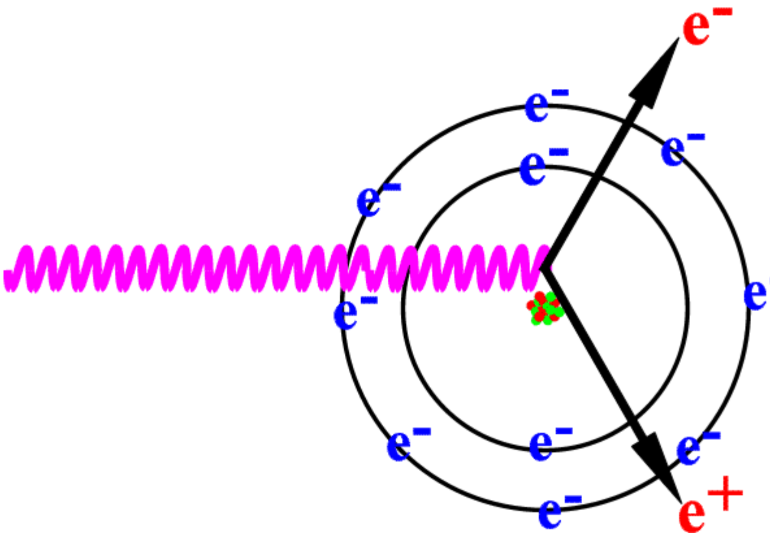

Figure 1.6: Pair production.

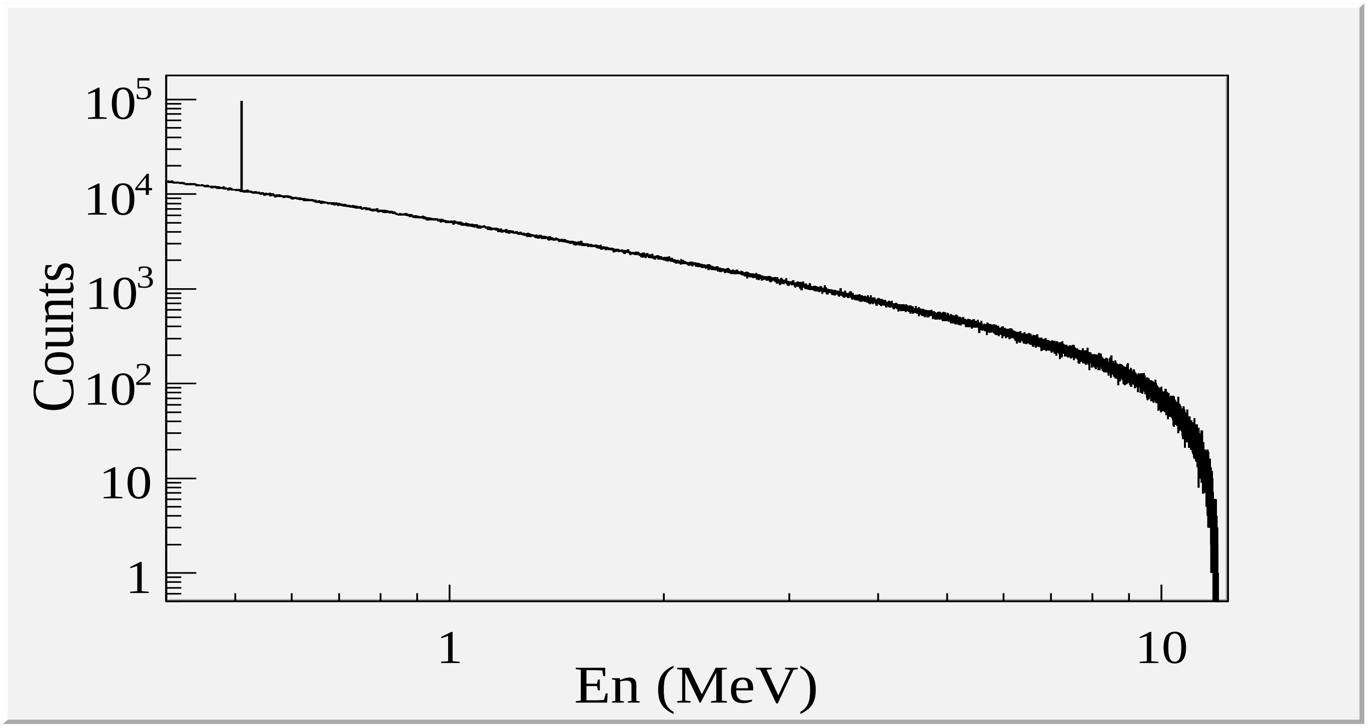

Figure 1.7: Photon spectrum of 12 MeV mono energy 10 million electrons impinge on a 1.016 mm thick tungsten target.

1.4 Emittance Measurement

Emittance is an important parameter in accelerator physics. When the emittance with Twiss parameters are given at the exit of the gun, one will be able to calculate beam size and divergence any given point along the beamline. To study the process of positron creation, one need to know the beam size and divergence on the target. Emittance with Twiss parameters are also key parameters for any accelerator simulations which will help one to understand the process and make predictions.

1.4.1 Emittance

In accelerator physics, Cartesian coordinate system was used to describe motion of the accelerated particles. Usually the z-axis of Cartesian coordinate system is defined to be along the electron beam line and describes longitudinal beam profile. The x-axis and y-axis are horizontal and vertical coordinates which constitute transverse beam profile. For the convenience of representation, one may use z to represent transverse coordinates and express longitudinal profile with natural coordinates s along the beamline. Transverse beam profile changes z is function of s, $z(s)$. The angle of a accelerated charge regarding the designed orbit can be defined as $z' = \frac{dz}{ds}$.

The phase space z vs. z' the beam is an ellipse with invariant area (along the beamline). This is called Courant-Snyder invariant [10]. The transverse emittance ϵ of the beam is defined to be the area of the ellipse, which contains 90% of the particles. Beam divergence and Twiss parameters related to the beam size and divergence by Eq. 1.5,

$$\sigma_x(s) = \sqrt{\epsilon_x(s)\beta_x(s)},\ \sigma_{x'}(s) = \sqrt{\epsilon_x(s)\gamma_x(s)}. \tag{1.5}$$

where is ϵ_x beam emittance, σ_x is rms beam size, $\sigma_{x'}$ is rms beam divergence and β_x and γ_x are two of the Twiss parameters.

1.4.2 Emittance Measurement

The HRRL beam emittance was measured using an Optical Transition Radiation (OTR). Transition radiation was theoretically predicted by Ginzburg and Frank [11] in 1946 to occur when a charged particle passes the boundary of two medium emits radiation. An Optical Transition Radiation (OTR) based viewer was installed to allow measurements at the high electron currents available using the HRRL at 15 MeV with 200 ns macro pulse width and 37.2 mA peak current. The visible is produced when a relativistic electron beam crosses the boundary of two mediums with different dielectric constants. Visible radiation is emitted at an angle of 90° with respect to the incident beam direction when the electron beam intersects the target at a 45° angle. These backward-emitted photons are observed using a digital camera and can be used to measure the shape and intensity of the electron beam based on the OTR distribution. Although an emittance measurement can be performed in a several ways [12, 13], the Quadrupole scanning method [14] was used to measure the emittance, Twiss parameters, and beam energy in this work.

1.4.3 Quadrupole Scanning Method

Fig. 1.8 illustrates the beamline components used to measure the emittance for the quadrupole scanning method. A quadrupole is positioned at the exit of the linac to focus or de-focus the beam as observed on the OTR view screen. The 3.1 m distance between the quadrupole and the screen was chosen in order to minimize chromatic effects and to satisfy the thin lens approximation. Assuming the thin lens approximation, $\sqrt{k_1}L << 1$, is satisfied, the transfer matrix of a quadrupole magnet may be expressed as

$$\mathbf{Q} = \begin{pmatrix} 1 & 0 \\ -k_1 L & 1 \end{pmatrix} = \begin{pmatrix} 1 & 0 \\ -\frac{1}{f} & 1 \end{pmatrix}, \tag{1.6}$$

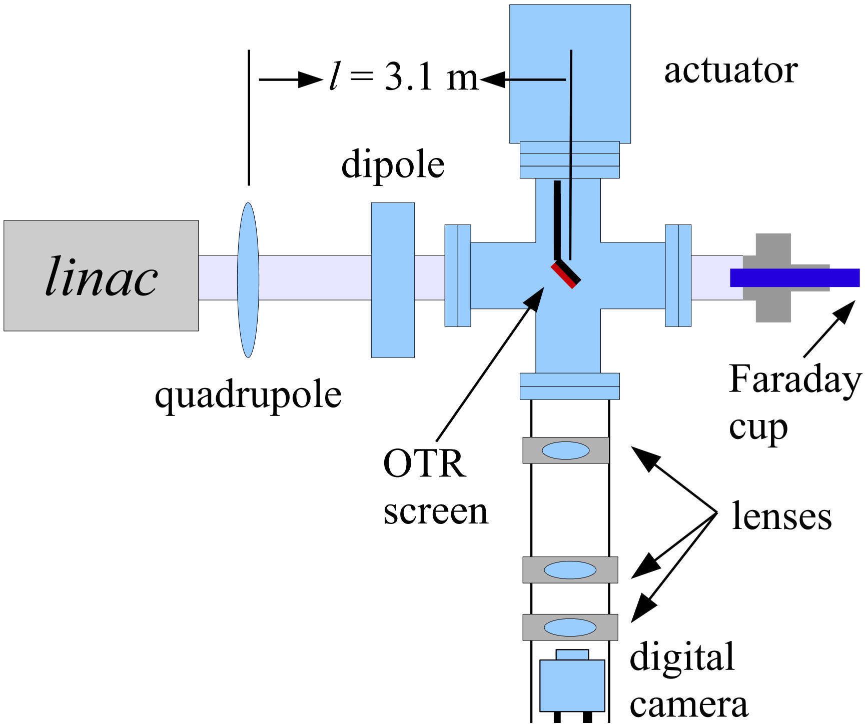

Figure 1.8: Apparatus used to measure the beam emittance.

where k_1 is the quadrupole strength, L is the length of quadrupole, and f is the focal length. A matrix representing the drift space between the quadrupole and screen is given by

$$\mathbf{S} = \begin{pmatrix} 1 & l \\ 0 & 1 \end{pmatrix}, \tag{1.7}$$

where l is the distance between the scanning quadrupole and the screen. The transfer matrix $\mathbf{M}$ of the scanning region is given by the matrix product $\mathbf{SQ}$. In the horizontal plane, the beam matrix at the screen ($\sigma_{\mathbf{s}}$) is related to the beam matrix of the quadrupole ($\sigma_{\mathbf{q}}$) using the similarity transformation

$$\sigma_{\mathbf{s}} = \mathbf{M}\sigma_{\mathbf{q}}\mathbf{M}^{\mathrm{T}}. \tag{1.8}$$

where the $\sigma_{\mathbf{s}}$ and $\sigma_{\mathbf{q}}$ are defined as [15]

$$\sigma_{\mathbf{s},x} = \begin{pmatrix} \sigma^2_{\mathrm{s},x} & \sigma_{\mathrm{s},xx'} \\ \sigma_{\mathrm{s},xx'} & \sigma^2_{\mathrm{s},x'} \end{pmatrix}, \ \sigma_{\mathbf{q},x} = \begin{pmatrix} \sigma^2_{\mathrm{q},x} & \sigma_{\mathrm{q},xx'} \\ \sigma_{\mathrm{q},xx'} & \sigma^2_{\mathrm{q},x'} \end{pmatrix}. \tag{1.9}$$

By defining the new parameters [14]

$$A \equiv l^2\sigma^2_{\mathrm{q},x}, \ B \equiv \frac{1}{l} + \frac{\sigma_{\mathrm{q},xx'}}{\sigma^2_{\mathrm{q},x}}, \ C \equiv l^2\frac{\epsilon^2_x}{\sigma^2_{\mathrm{q},x}}, \tag{1.10}$$

the matrix element $\sigma^2_{\mathrm{s},x}$, the square of the rms beam size at the screen, may be expressed as a parabolic function of the product of k_1 and L

$$\sigma^2_{\mathrm{s},x} = A(k_1L)^2 - 2AB(k_1L) + (C + AB^2). \tag{1.11}$$

The emittance measurement was performed by changing the quadrupole current, which changes k_1L, and measuring the corresponding beam image on the view screen. The measured two-dimensional beam image was projected along the image's abscissa and ordinate axes. A Gaussian fitting function is used on each projection to determine the rms value, σ_s in Eq. (1.11). Measurements of σ_s for several quadrupole currents ($k_1 L$) is then fit using the parabolic function in Eq. (1.11) to determine the constants A, B, and C. The emittance (ϵ) and the Twiss parameters (α and β) can be found using Eq. (1.12).

$$\epsilon = \frac{\sqrt{AC}}{l^2},\ \beta = \sqrt{\frac{A}{C}},\ \alpha = \sqrt{\frac{A}{C}}(B + \frac{1}{l}). \tag{1.12}$$

== Apparatus ==

Chapter 2

Apparatus

2.1 HRRL Beamline

The first step of this experiment is to deliver an electron beam with energy around 10 MeV and with sufficient current to the tungsten foil. A 16 MeV S-band High Repetition Rate Linac (HRRL) located at the Beam Lab of the Department of the Physics, Idaho State University is used to generate incident electron beam. The energy of the HRRL can be tunable between 3 to 16 MeV and its rep and its repetition rate is tunable between 1-300 Hz. Some basic parameters of the HRRL is given in the 2.1. HRRL cavity is shown in Fig. 2.1. It has a thermionic gun and two sets of steering magnets and two sets of solenoid magnets.

To construct a beamline can run on both positron and electron mode, the cavity is relocated to its current position and quadrupole and dipole magnets to transport the beam. As shown in Fig. 2.2 and described in Tab. 2.2 more diagnostic tools like OTR/YAG screens, Faraday cups and toroids are installed to the new beamline for diagnostic purposes of electron beam. Energy slits are added to the beamline for the control of energy/momentum spread of

Table 2.1: Emittance Measurement Results.

Parameter	Unit	Value
maximum energy	MeV	16
peak current	mA	100
repetition rate	Hz	300
absolute energy spread	MeV	2-4
macro pulse length	ns	>50

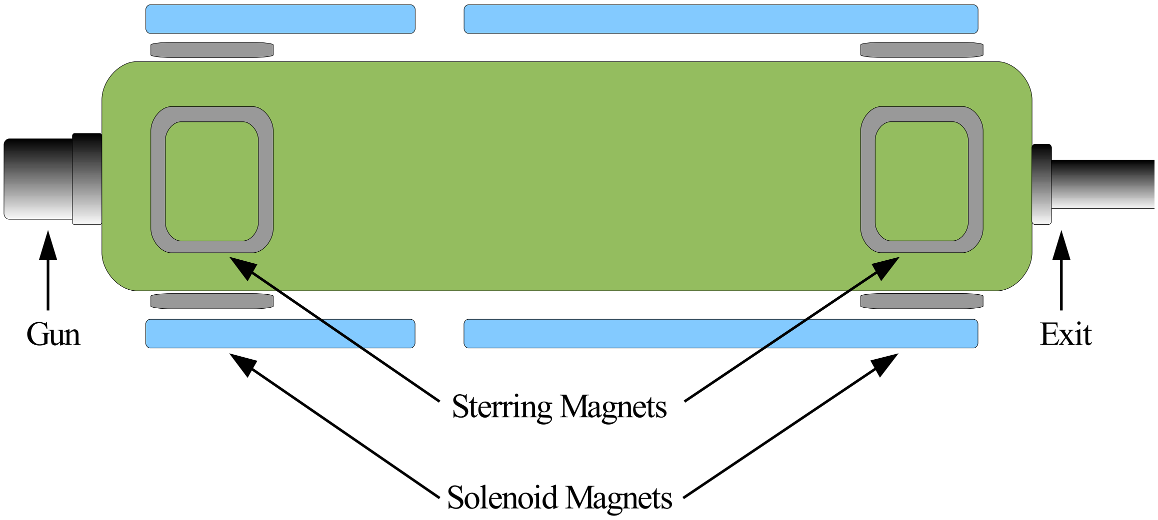

Figure 2.1: HRRL cavity.

the beam. A insertable tungsten foil target (T1) is placed between the 1st and 2nd triplets to produce positrons when the electron beam hits it.

2.2 The OTR Imaging System

The OTR target is 10 μm thick aluminum foil with a 1.25 inch diameter. The OTR is emitted in a cone shape with the maximum intensity at an angle of $1/\gamma$ with respect to the reflecting angle of the electron beam [**?**]. Three lenses, 2 inches in diameter, are used for the imaging system to avoid optical distortion at lower electron energies. The focal lengths and position of the lenses are shown in Fig. 2.3. The camera used was a JAI CV-A10GE digital camera with a 767 by 576 pixel area. The camera images were taken by triggering the camera synchronously with the electron gun.

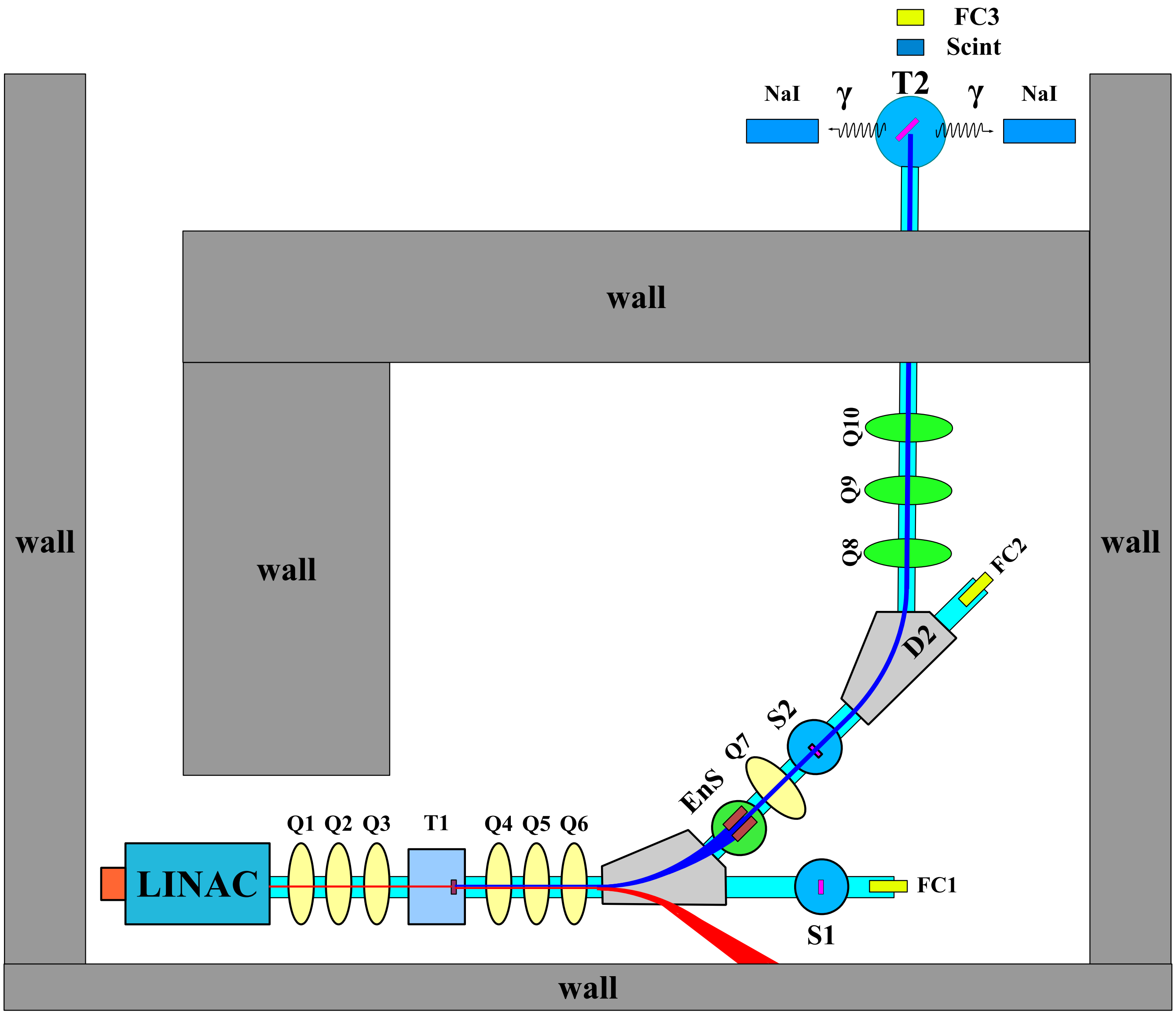

Figure 2.2: HRRL beamline layout and parts.

Table 2.2: HRRL Beamline Parts and Coordinates.

Label	Beamline Element	Distance from Linac Exit (mm)
Q1	quadrupole	335
Q2	quadrupole	575
Q3	quadrupole	813
T1	e^+ production target	1204
Q4	quadrupole	1763
Q5	quadrupole	2013
Q6	quadrupole	2250
D1	dipole	2680
S1	OTR screen	
FC1	Faraday cup	
EnS	energy slit	
S2	YAG screen	
Q7	quadrupole	3275
D2	dipole	3842
FC2	Faraday cup	
Q8	quadrupole	4044
Q9	quadrupole	4281
Q10	quadrupole	4571
T2	annihilation target	7381

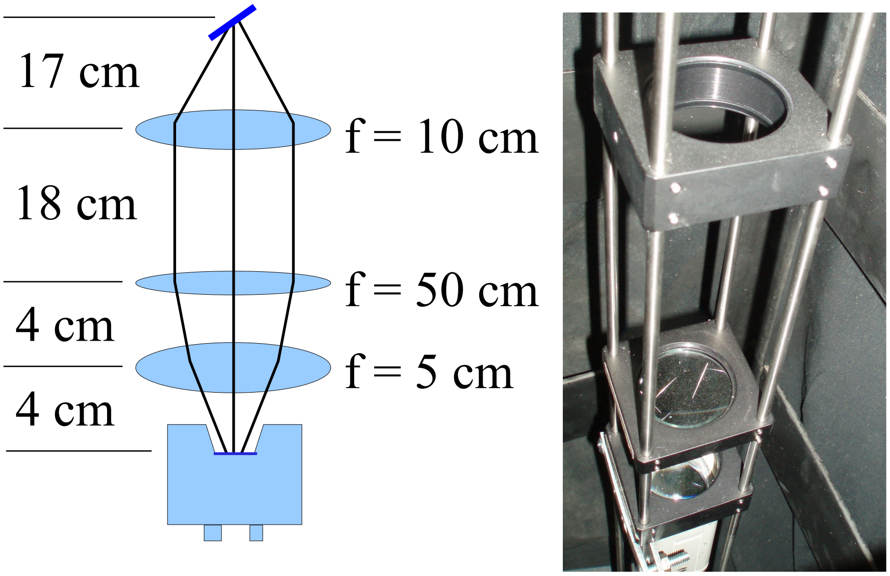

Figure 2.3: The OTR Imaging system.

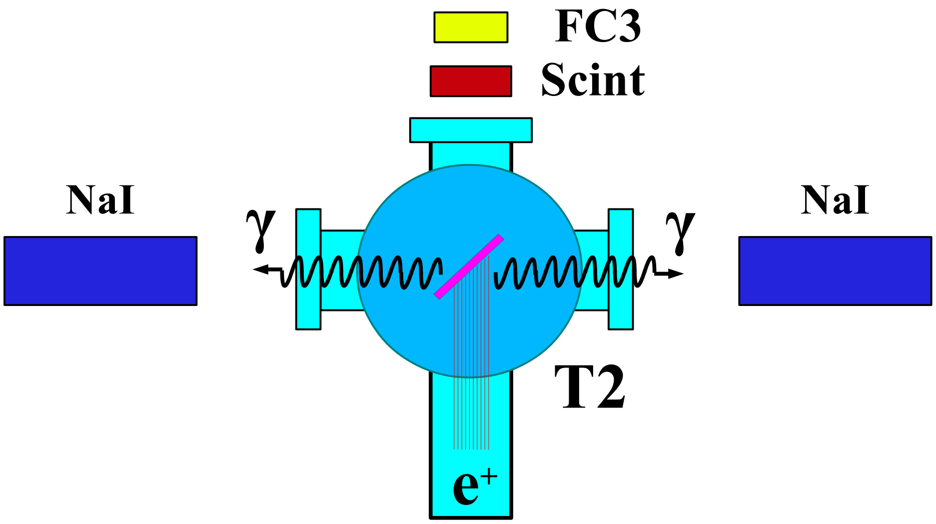

Figure 2.4: Positron Detection System. T2 (pink) is 45 degree placed with horizontal plane, then rotated towards left detector 45 degree.

2.3 Positron Detection

Positrons are transported to the end of the 90 degree beamline located on the experimental side of the room that is shielded from the background noises. A 6-way cross is placed at the end of the beamline to hold T2 and thin windows. Two NaI detectors are used to detect photons produced when positrons from the beam annihilated in T2. The setup is shown in Fig. 2.4. A scintillator and a Faraday cup are at the end of the beam line and used to maximize the positron with electron beam respectively. Positrons reach T2 can thermalized inside T2 and then annihilate. During the thermalization a positron loses its kinetic energy and when it annihilates with an electron, two 511 keV photons are emitted back to back. Two NaI detectors and accelerator RF pulse are in coincidence mode to eliminate noises.

2.3.1 NaI Detectors

NaI crystals, shown as in Fig. 2.6, were used to detect 511 keV photons from positron annihilation. Originally, the detectors had pulse length around 400 μs. Resistors and capac-

Table 2.3: Radioactive sources and photon peaks.

Radioactive Sources	Unit	First Peak	Second Peak
Co-60	keV	1173	1332
Na-22	keV	511	1275

itors added to PMT bases and pulse length is shorten to less than 1 μs. The NaI detector have one dynode and one anode outputs. PMT base configuration of the NaI detector is shown in the Fig. 2.5 and bases made shown in Fig. 2.7. The crystal is SAINT-GOBAIN CRYSTAL & DETECTORS (MOD. 3M3/3) NaI crystal with sizes of 3" × 3". PMT base take HV around -1150 V. It takes ADC 5.7 μs to convert analog signal to digital signal. The signal from anode was delayed 6 μs by long cable and sent to the ADC.

Bases were calibrated using Na-22 and Co-60 sources with photon peaks indicated in the Table 2.3. The Fig. 2.8 is the oscilloscope image of Co-60 photon pulses incident on the detector. The calibrated NaI detector spectrum of Na-22 and Co-60 sources is shown in Fig. 2.9. The rms values of the fits on the four peaks shown in the Fig. 2.9 are $\sigma_{Na,511} = 18.28 \pm 0.04$ MeV, $\sigma_{Na,1275} = 44.51 \pm 0.27$ MeV, $\sigma_{Co,1173} = 42.49 \pm 0.24$ MeV, and $\sigma_{Co,1332} = 50.30 \pm 0.39$ MeV.

2.3.2 Trigger for DAQ

The trigger for DAQ required a coincidence between one or more NaI detectors and the electron accelerator gun pulse. The last dynode signals from left and right NaI detectors were inverted using a Ortec 474 amplifier and sent to a Constant Fraction Discriminator (CFD Model specs). RF noise from the accelerator is as large as the signal from the NaI detector. Since it is correlated in time with the gun pulse, the gun pulse was used to generate a VETO pulse that prevent the CFD from triggering on this RF noise. After this discrimination and RF noise rejection, the discriminated dynode signals were sent to an Octalgate Generator (Model) that increased the width of the logic signals to prevent multiple pulses during a single electron pulse. Then the signals were sent to Quad Coincidence to generate AND

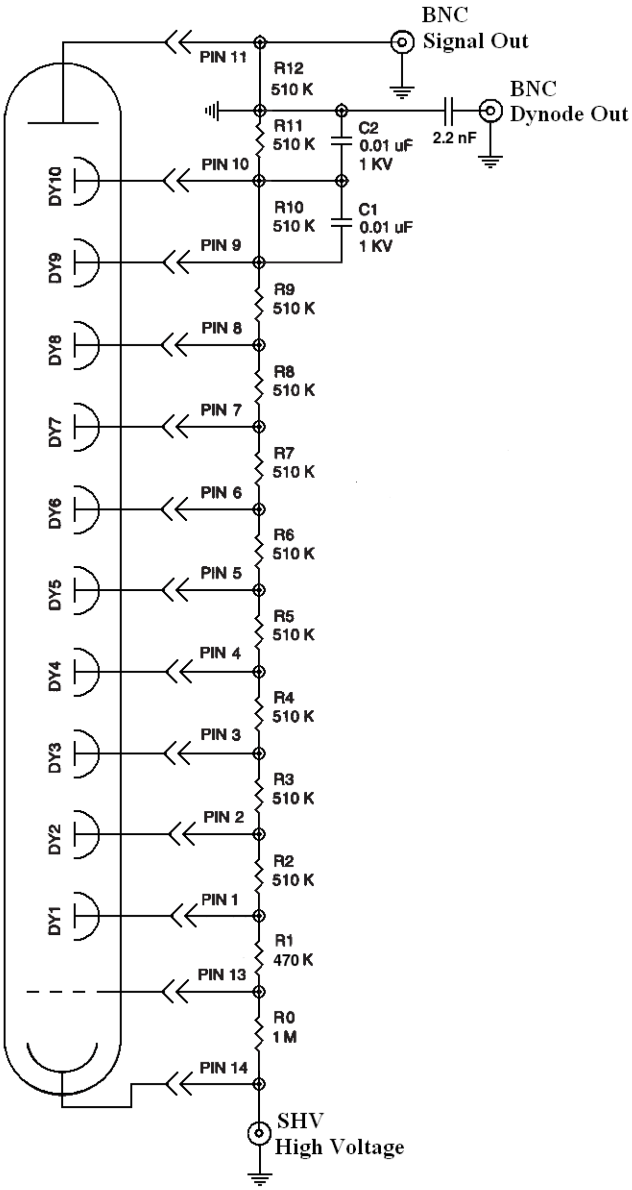

Figure 2.5: Modified PMT base design.

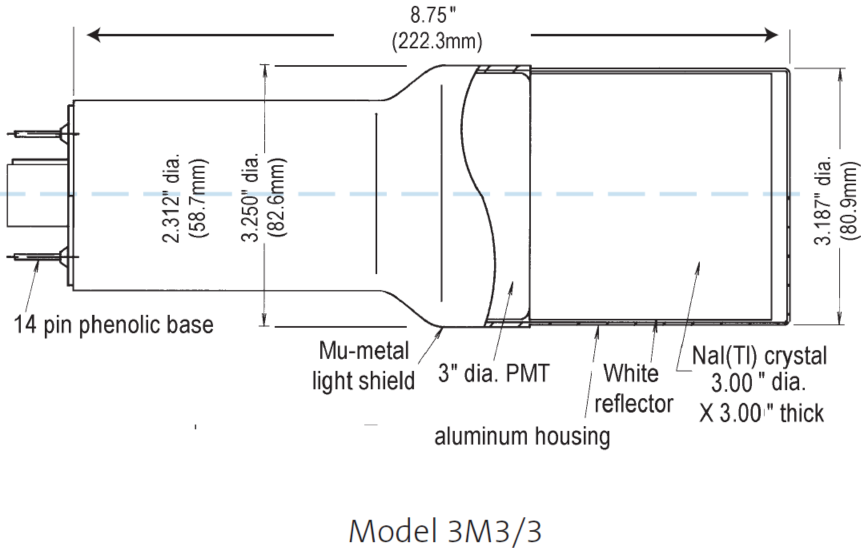

Figure 2.6: NaI crystal dimension.

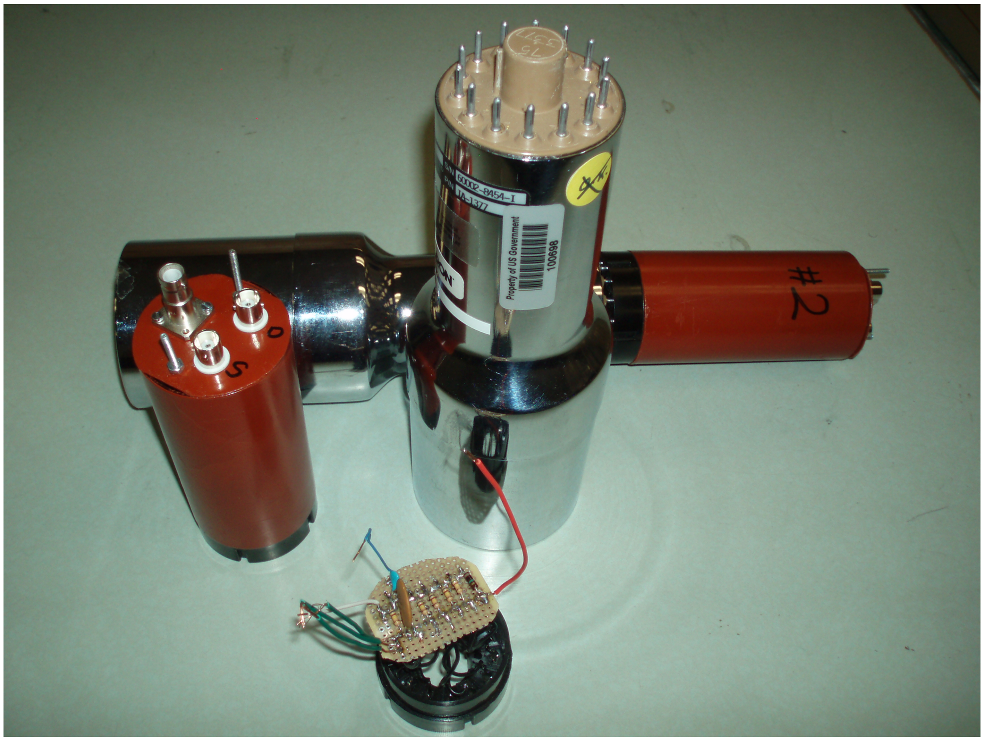

Figure 2.7: NaI crystals and new bases.

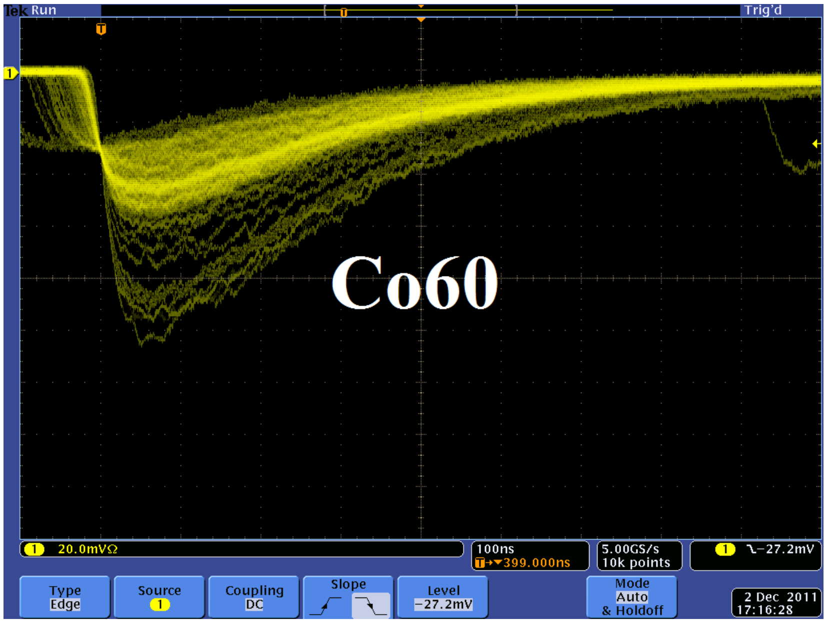

Figure 2.8: Pulses from Co-60 source observed on the scope. The amplitude is about 60 mV. The rise time is larger than 50 ns, and the fall time is larger than 700 ns.

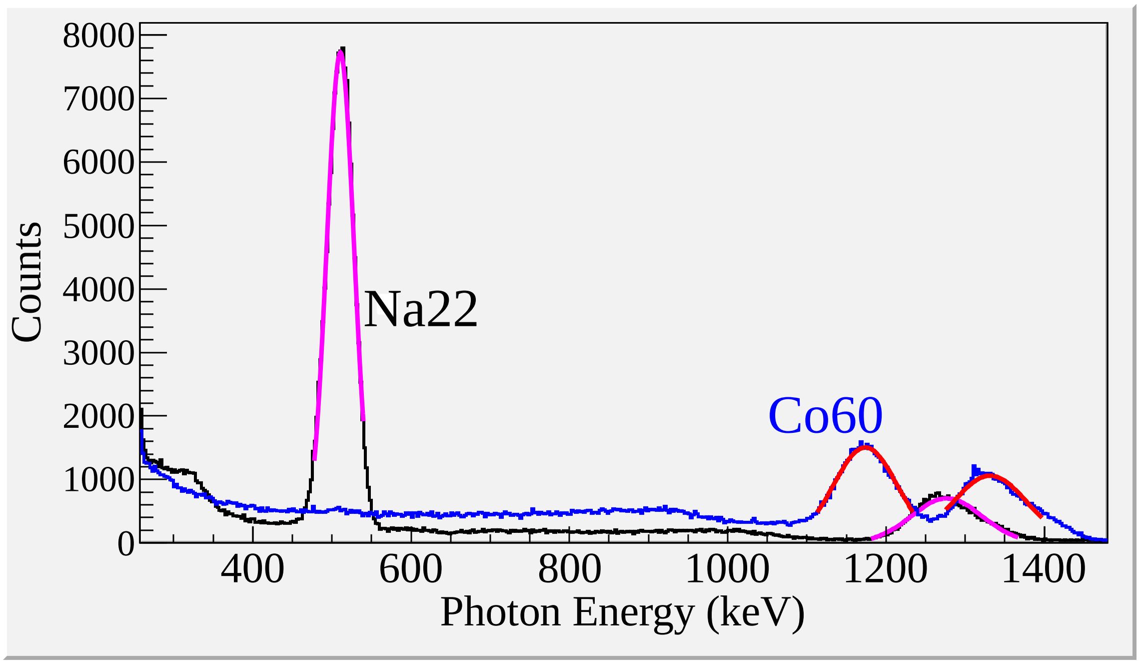

Figure 2.9: Calibrated NaI spectrum of Na-22 and Co-60 sources.

logic between electron gun and dynode signals. The logic is set as:

$$(NaI\ Left\ \&\&\ Gun\ Trigger)\ \&\&\ (NaI\ Rgiht\ \&\&\ Gun\ Trigger). \tag{2.1}$$

This is to make sure we have trigger when photons back to back scatter to the NaI detectors when electron gun is on. Then this trigger was sent to ORTEC Gate & Delay Generator. One of the out from gate generator was used to generate a gate to read analog signal from anode. Another output was delayed by 6 μs, necessary time to convert the analog signal from anode to digital signal, and used as trigger for the DAQ.

== Simulation ==

Chapter 3

Simulation

A simulation was performed using the package G4beamline(ref Muons inc) to study the processes of position generation and transportation. ”G4beamline is a particle tracking and simulation program based on the Geant4 (reference G4) toolkit that is specifically designed to easily simulate beamlines and other systems using single-particle tracking.” Since the ratio of e^+/e^- during the positron generation process is very low (on the order of 0.001) and the positron beam loss during the transportation is large, it was necessary to divide whole process into 5 steps. A new beam event generator is created based on the results of the previous step in the simulation. The first step generates electrons according to a measurement made of the accelerator that was used in the experiment. Electrons are transported to T1 in vacuum and as a result the interactions of the electron with T1 produce positrons. The second step is the transportation of the positrons generated at T1 to the entrance of first dipole magnet. The third step is the transportation of the positrons from the entrance of the first dipole magnet to the end of the second dipole. The fourth step is the transportation of the beam from the exit of the second dipole to the T2 target. The fifth step is the positron beam interaction with T2 and detection of the resulting 511 keV photons.

3.1 Step 1 - The Electron Beam Generation and Transpiration to T1

In this step, an electron beam is generated from the experimental measure electron beam parameters. The Twis parameters described in the earlier chapter used electron generated

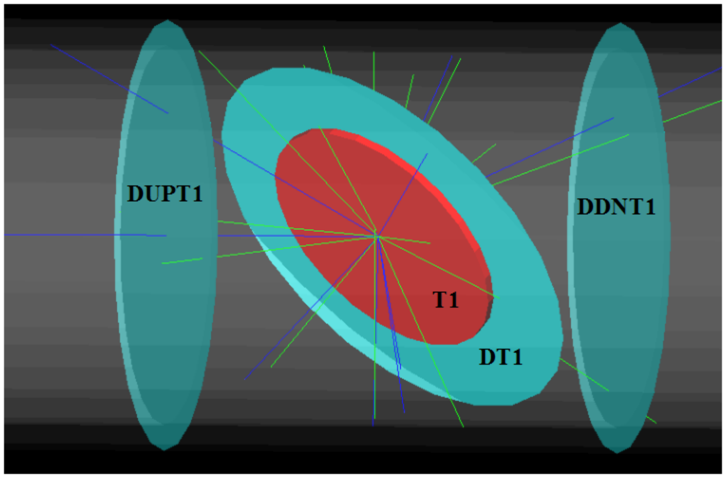

Figure 3.1: T1 is positron production target with same geometry and material as real target. DUPT1 is virtual detector located upstream to sample incoming electron beam. DDNT1 is down stream virtual detector; DT1 is a virtual detector that is placed right after T1 with same angle as T1.

the beam. The energy distribution is of the beam is measured and shown in the Fig. 4.4. The blue dots are measurements and red line are the fit composed of two skewed Gaussian distributions. The fit parameters are given in the Table 4.2 in the previous chapter.

Series of virtual detectors are placed along the beamline to sample the beam. As an example, in the Fig. 3.1 shown are three detectors and the T1. The electron beam is observed at DUPT1 (Detector 25.52 mm UPstream of T1) and positrons (or electrons and photons) generated during the interaction of electron beam with T1 are observed at DT1 (Detector of T1) and DDNT1 (detector DowN 25.52 mm stream of T1).

3.1.1 Positron Beam on DDNT1

In simulation, 13,799,743,900 electrons with energy distribution shown in black line in Fig. 3.2 incident on T1 created positrons represented by red line. The blue line is electrons detected at downstream of T1. In Fig. 3.2 only 1000th of the total number of the particles is shown due to the large size. The Incident electrons detected on DUPT1 and downstream

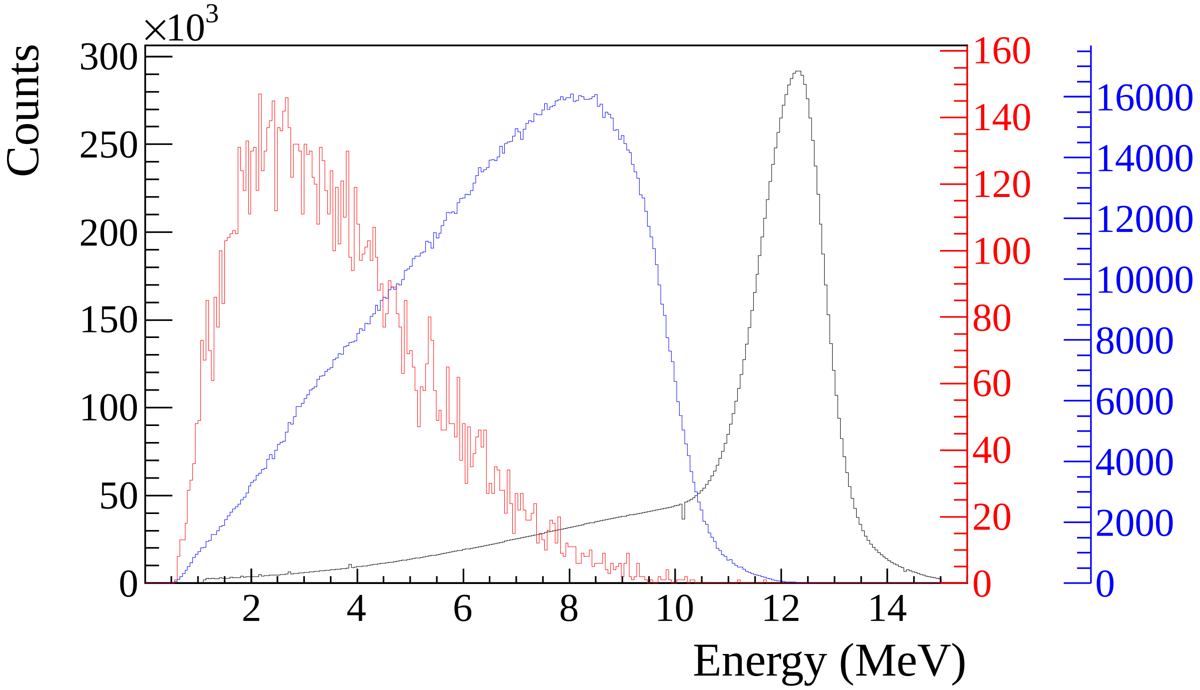

Figure 3.2: Energy distribution of incident electrons (black), electrons after T1 (blue) and created positrons (red).

positrons and electrons detected on DDNT1.

As can be seen on Fig. 3.3 (b) and (c) The y spacial distribution and y divergence distribution of the beam has sharp drops on their left side. The *y vs. x* distribution of the beam shown in Fig. 3.3 (e) and Fig. 3.3 (f) is zoomed in version of 3.3 (e). has a sharp drop in the region between -25.8 mm and -27.2 mm that corresponds to the boundary of the target T1. Fig. 3.4 shows the geometry of the target T1 and the sensitive detector DDNT1. If the target size was increased, it would eventually intersected the detector DDNT1 at a distance of 25.8 mm from the beam center. A 1.4 mm wide stripe of low counts is visible on DDNT1 that is a result of the target's thickness of 1.016 mm and the 45° angle of intersection $(1.016\sqrt{2} = 1.44)$. The edge of the target does not produce many positrons compared to the face of the target, and as a result you see the stripe.

As shown in Figs. 3.5 (a) and (b), the spacial distribution on Y decrease occures at $\theta = 45°$. Positrons are emitted from both the downstream and upstream side of the target. As

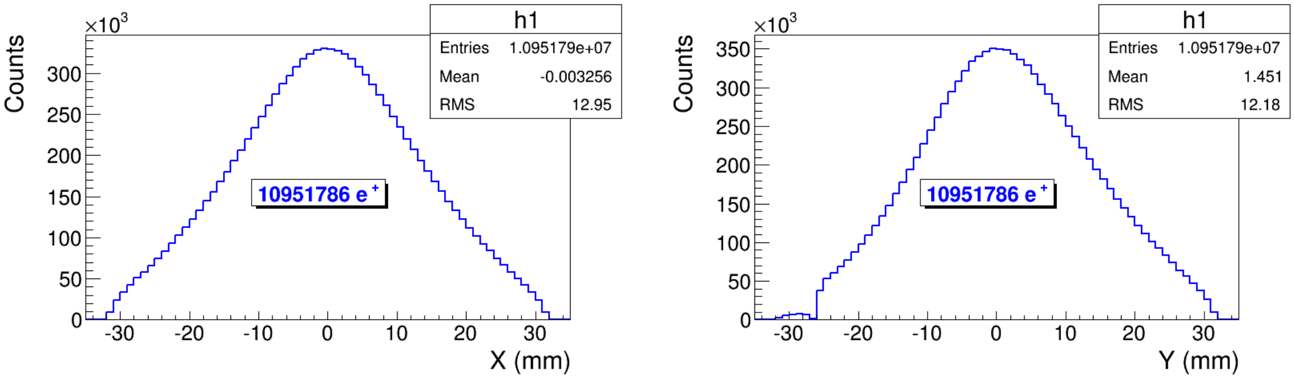

(a) X DDNT1 (b) Y DDNT1

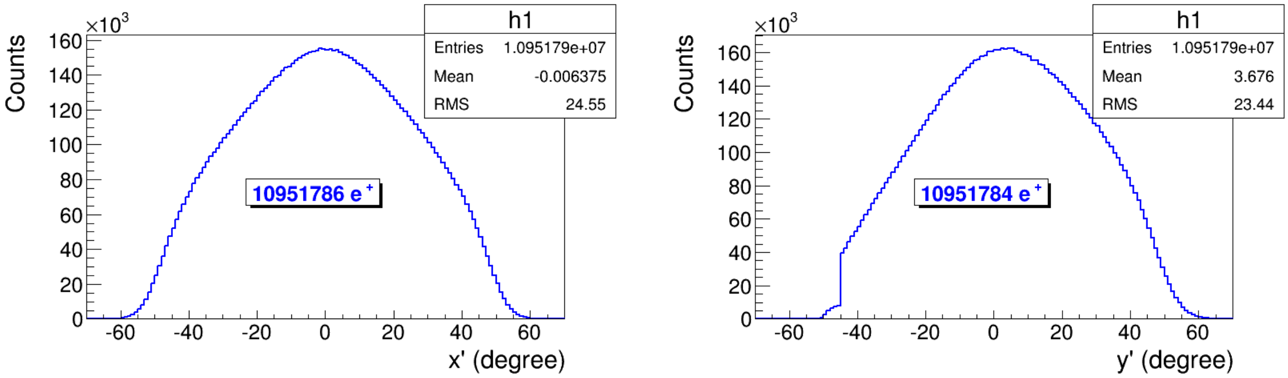

(c) X' DDNT1 (d) Y' DDNT1

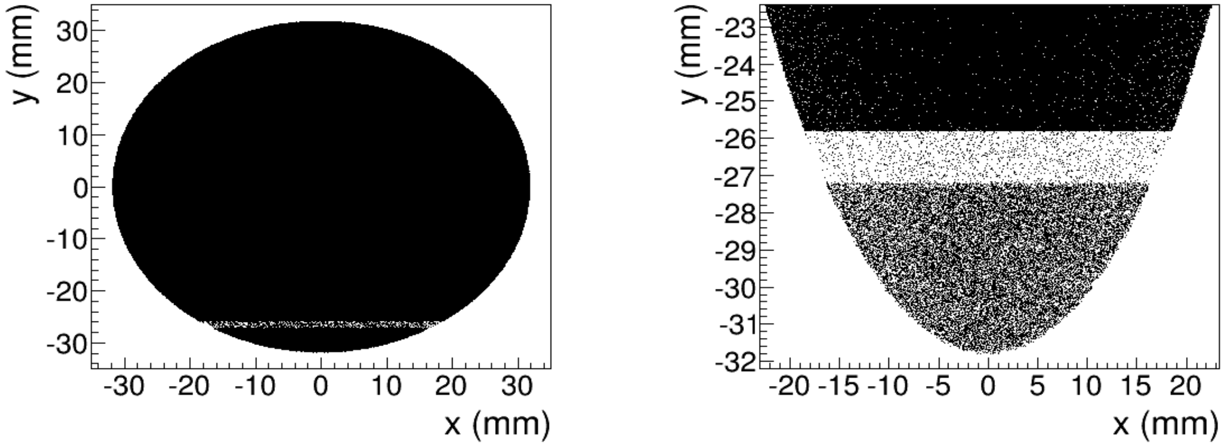

(e) X *vs.* Y DDNT1 (f) X *vs.* Y DDNT1 zoom

Figure 3.3: Transverse spacial and angular distribution of positrons on the virtual detector DDNT1.

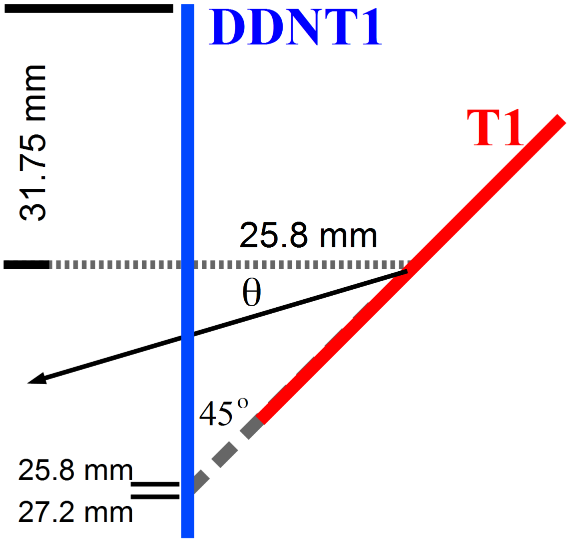

Figure 3.4: Geometry of the target T1 and the virtual detector DDNT1.

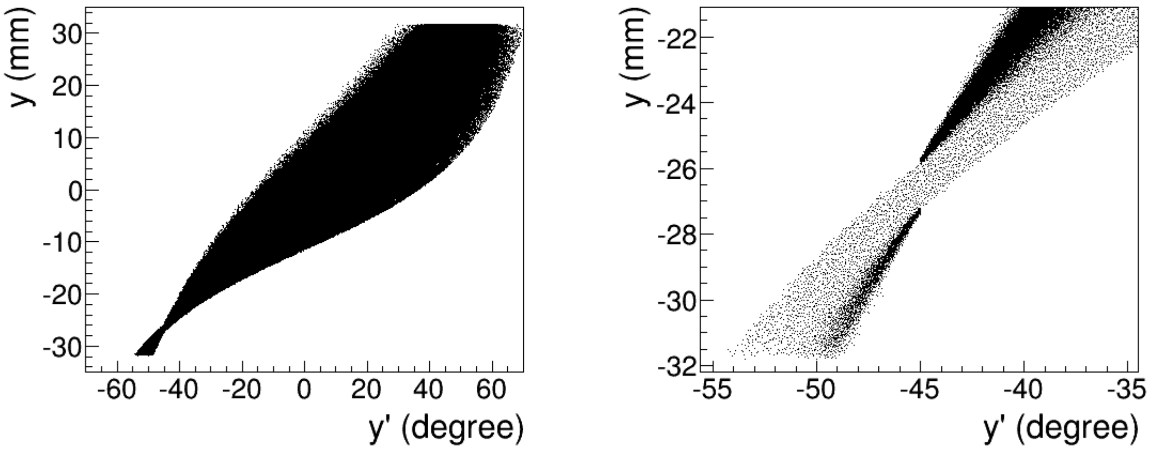

(a) Y' *vs.* Y.

(b) Y' *vs.* Y zoom.

Figure 3.5: Positron beam distribution Y divergence vs. Y spacial distribution on DDNT1.

shown in the figure, positrons from the downstream side of the target intersect the detector at angles below 45° while positrons from the upstream side of the target begin to hit the detector at angles beyond 45°. The 1.4 mm gap represents the transition of positrons between these two extremes.

3.1.2 Positron Beam on DQ4 and DD1

Resulted positron beam energy distribution on virtual detectors that are placed at the entrance of Q4 (DQ4) and D1 (DD1UP) are shown in Fig. 3.6. Nearly 90% positrons are lost when transported from DQ4 to DD1UP due to the large divergence of positrons.

3.2 Step 2 - Transportation of the The Positron Beam after T1 to The Entrance of The First Dipole

In this step, the positrons generated in the first step divided into 1 keV/c momentum bins. Higher energy positrons tend to have smaller polar angle and vise versa. Because of this correlation, positrons in different momentum bins have different angular distribution.

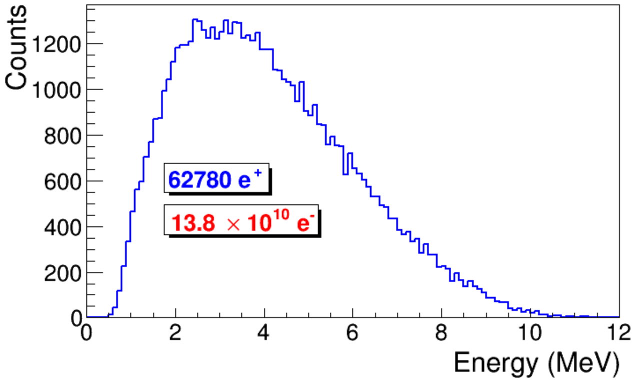

(a) Positron energy distribution on DQ4

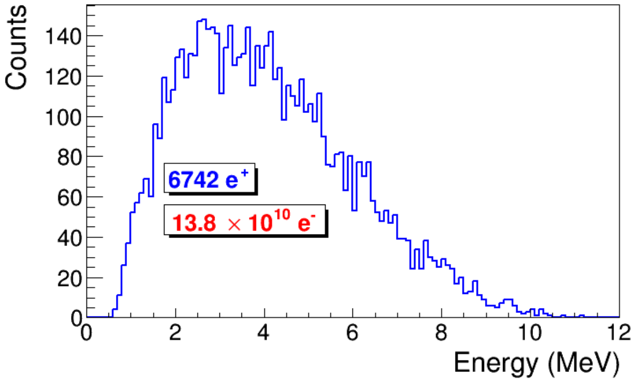

(b) Positron energy distribution on DD1

Figure 3.6: Positron beam energy distribution detected on the downstream of T2.

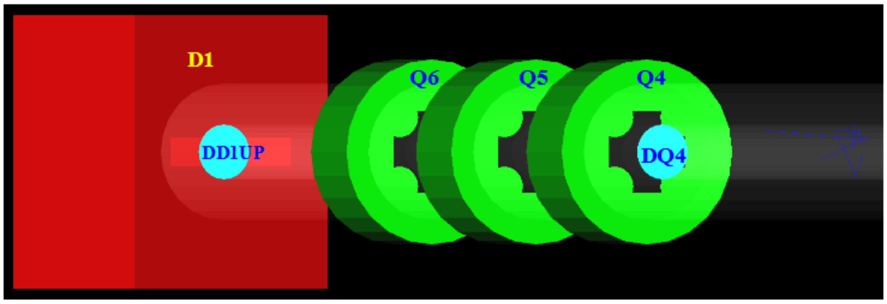

Figure 3.7: Magnets and virtual detectors used in step 2.

Keeping this correlation in mind, in step 2, each momentum bin is sampled individually. Each momentum bin is an independent beam source that generates positrons with individual weights, spacial and angular distributions. Positrons generated at downstream T1 (at detector DDNT1) and transported to entrance of the D1 as shown in the Fig 3.7. Virtual detectors are placed at the entrance of Q4 (DQ4) and D1 (DD1UP) to track positrons. Beam detected at DD1UP is sampled for the generation of positron for the next step.

3.3 Step 3 - Generation of Positrons at the Entrance of the First Dipole and Their Transporting and Detection

In this step, positrons are generated at the entrance of the first dipole (on DD1UP shown in Fig. 3.7) by sampling the beam at the same location in previous step. Beam then

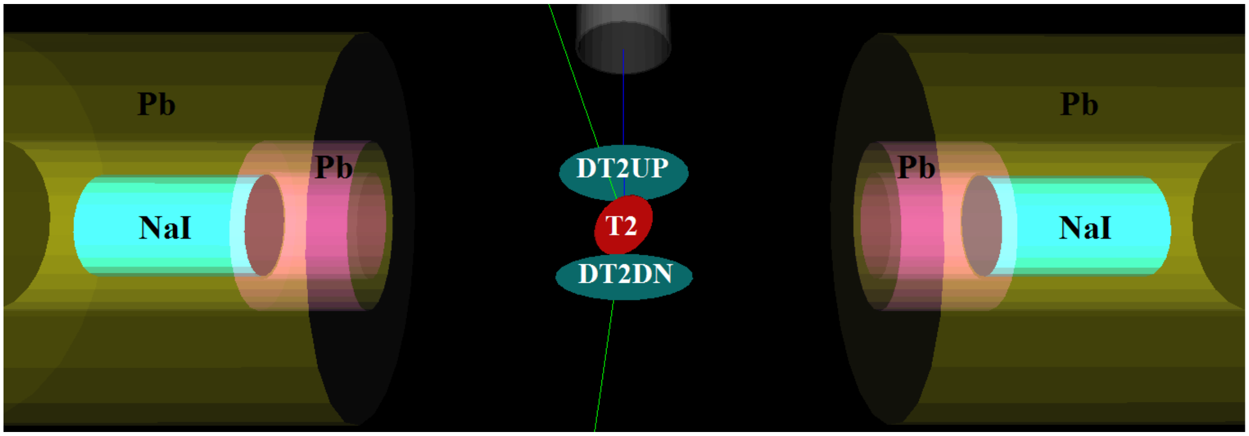

Figure 3.8: T2 and virtual detectors located upstream (DT2UP) and downstream (DT2DN) of T2. NaI dettectos and Pb shielding.

transported down to T2 located at the end the beamline as shown in Fig. 3.8. Two virtual detectors with 48 mm diameter (inner diameter of the beam pipe) are placed to upstream and downstream of T2 to detected incoming positrons and particles after T2. Two virtual detectors with same diameter as T2 placed next to two sides of T2. They are placed with same angle to the beam orientation as T2. NaI virtual detectors are placed horizontally to detect photons 170 mm away from the beamline center. 2 inches thick Pb shielding are placed around NaI detectors with circular openings with 2 inches diameter facing T2. When a positron annihilate inside T2, two back to back scattered 511 keV photons are generated with same event number. NaI detectors count 1 event when they both detect 511 keV photons with same event number.

3.3.1 Detector Efficiency

According to the detector efficiency chart, shown if Fig. 3.9 obtained from SAINT-GOBIAN CRYSTALS [18], at 511 keV, NaI crystals has 68% efficiency. If two detectors are operated in coincidence mode, the detection efficiency is $68\% \times 68\% = 46.24\%$.

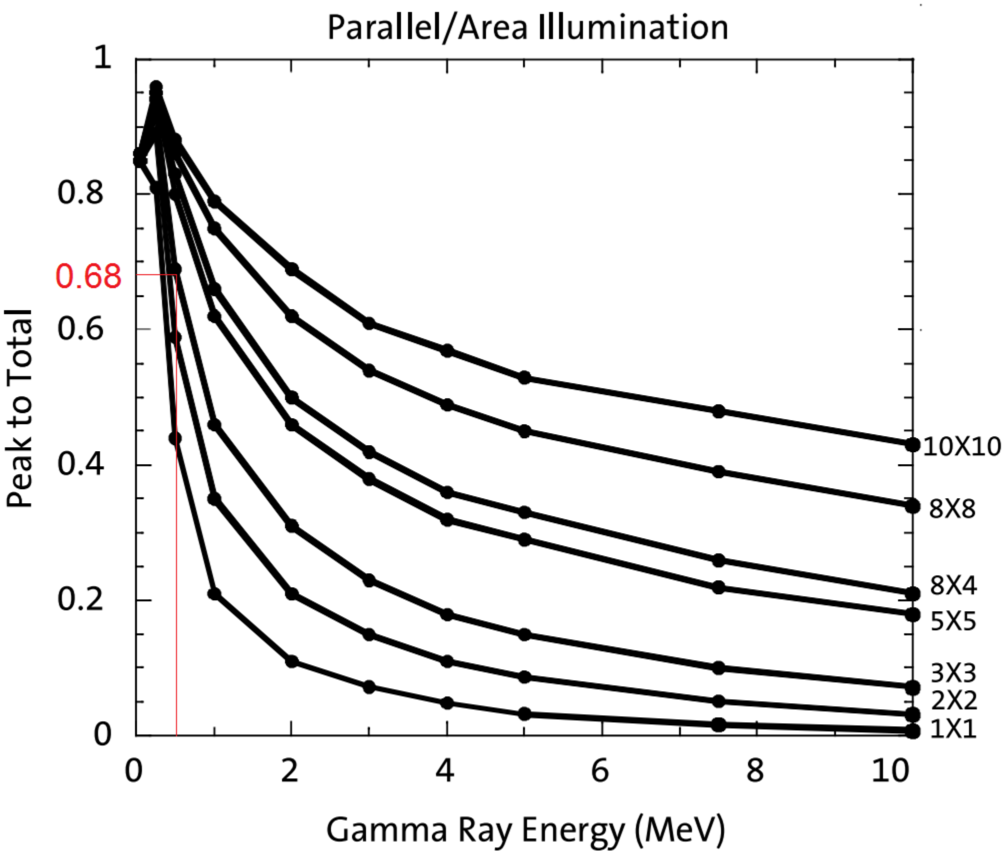

Figure 3.9: NaI detector efficiency obtained from SAINT-GOBIAN CRYSTALS [18].

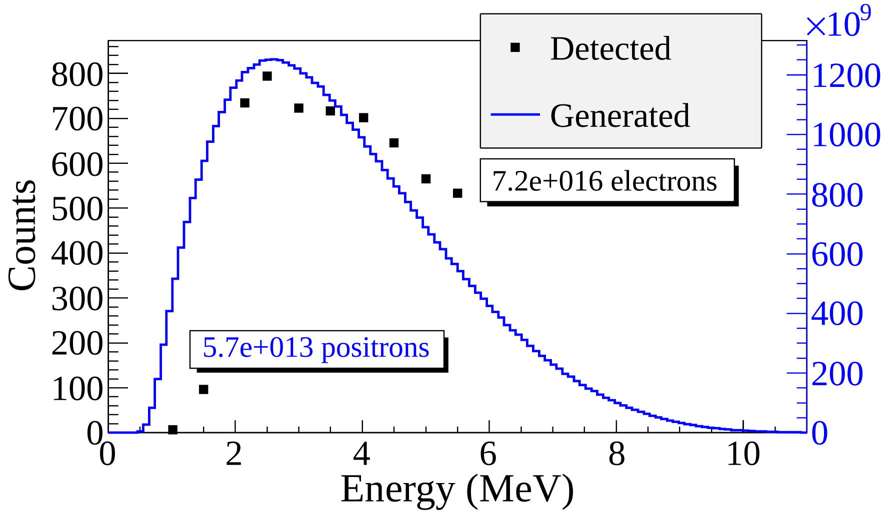

Figure 3.10: Positrons generated detected on virtual detector DDNT1 and 511 keV counts detected by NaI detectors in coincidence mode.

3.3.2 Positrons Detected by Detection System.

Positrons generated

3.3.3 Beam Loss Study

Positrons are generated by 7.253×10^{16} electrons incident on T1 and 5.756×10^{13} generated positrons. The transported positrons detected along the beamline. The beam lost is shown in Table 3.1 and Fig. 3.11. Detector efficiency is taken into consideration with coincidence mode.

As it can be seen from the 3.1, the counts of positron energy bins are in the order of 10^{12} at virtual detector DDNT1 (25.8 mm after T1). At the entrance of Q4, the counts drops two order of magnitude. This is due the solid angle the entrance of Q4 makes. The distance between T2 and the virtual detector at the entrance of Q4 is $d = 560$ mm, and the radius of virtual detector (which is inner diameter of beampipe) is $r = 24$ mm. The solid angle the virtual detector at the entrance of Q4 make is $\Omega_{\mathrm{q4}} = \frac{\pi r^2}{d^2} = \frac{\pi 24^2}{560^2}$. Positrons make up a cone with 45 degree half angle and the solid angle they make is $\Omega_{\mathrm{beam}} = 0.6\pi$. The ratio the

Table 3.1: Predicted Number Positrons of Transported and Number of 511 keV Photons Detected.

Energy (MeV)	On DDNT1	Enter Q4	Enter D1	Exit D1	Enter Q7	Enter D2	Exit D2	Reach T2	NaI
1.02 ± 0.25	2.5×10^{12}	1.4×10^{10}	1.4×10^{9}	1.2×10^{8}	2.6×10^{7}	2.7×10^{6}	1.2×10^{6}	4.3×10^{3}	7
1.50 ± 0.25	4.9×10^{12}	2.8×10^{10}	2.8×10^{9}	1.8×10^{8}	9.1×10^{7}	2.7×10^{7}	1.2×10^{7}	5.1×10^{4}	97
2.15 ± 0.25	6.5×10^{12}	3.8×10^{10}	3.8×10^{9}	3.8×10^{8}	1.7×10^{8}	7.8×10^{7}	3.6×10^{7}	4.4×10^{5}	734
2.50 ± 0.25	6.8×10^{12}	4.1×10^{10}	4.1×10^{9}	4.4×10^{8}	2.3×10^{8}	1.1×10^{8}	5.0×10^{7}	4.6×10^{5}	794
3.00 ± 0.25	6.6×10^{12}	4.1×10^{10}	4.1×10^{9}	4.6×10^{8}	2.7×10^{8}	1.3×10^{8}	6.1×10^{7}	4.5×10^{5}	723
3.50 ± 0.25	6.1×10^{12}	3.9×10^{10}	3.9×10^{9}	4.4×10^{8}	2.8×10^{8}	1.4×10^{8}	6.7×10^{7}	4.4×10^{5}	716
4.02 ± 0.25	5.3×10^{12}	3.5×10^{10}	3.5×10^{9}	4.1×10^{8}	2.7×10^{8}	1.4×10^{8}	6.9×10^{7}	4.3×10^{5}	702
4.50 ± 0.25	4.6×10^{12}	3.1×10^{10}	3.1×10^{9}	3.6×10^{8}	2.5×10^{8}	1.3×10^{8}	6.7×10^{7}	4.0×10^{5}	646
5.00 ± 0.25	3.8×10^{12}	2.7×10^{10}	2.7×10^{9}	3.1×10^{8}	2.2×10^{8}	1.2×10^{8}	6.2×10^{7}	3.6×10^{5}	566
5.50 ± 0.25	3.0×10^{12}	2.2×10^{10}	2.2×10^{9}	2.6×10^{8}	1.9×10^{8}	1.0×10^{8}	5.6×10^{7}	3.3×10^{5}	533

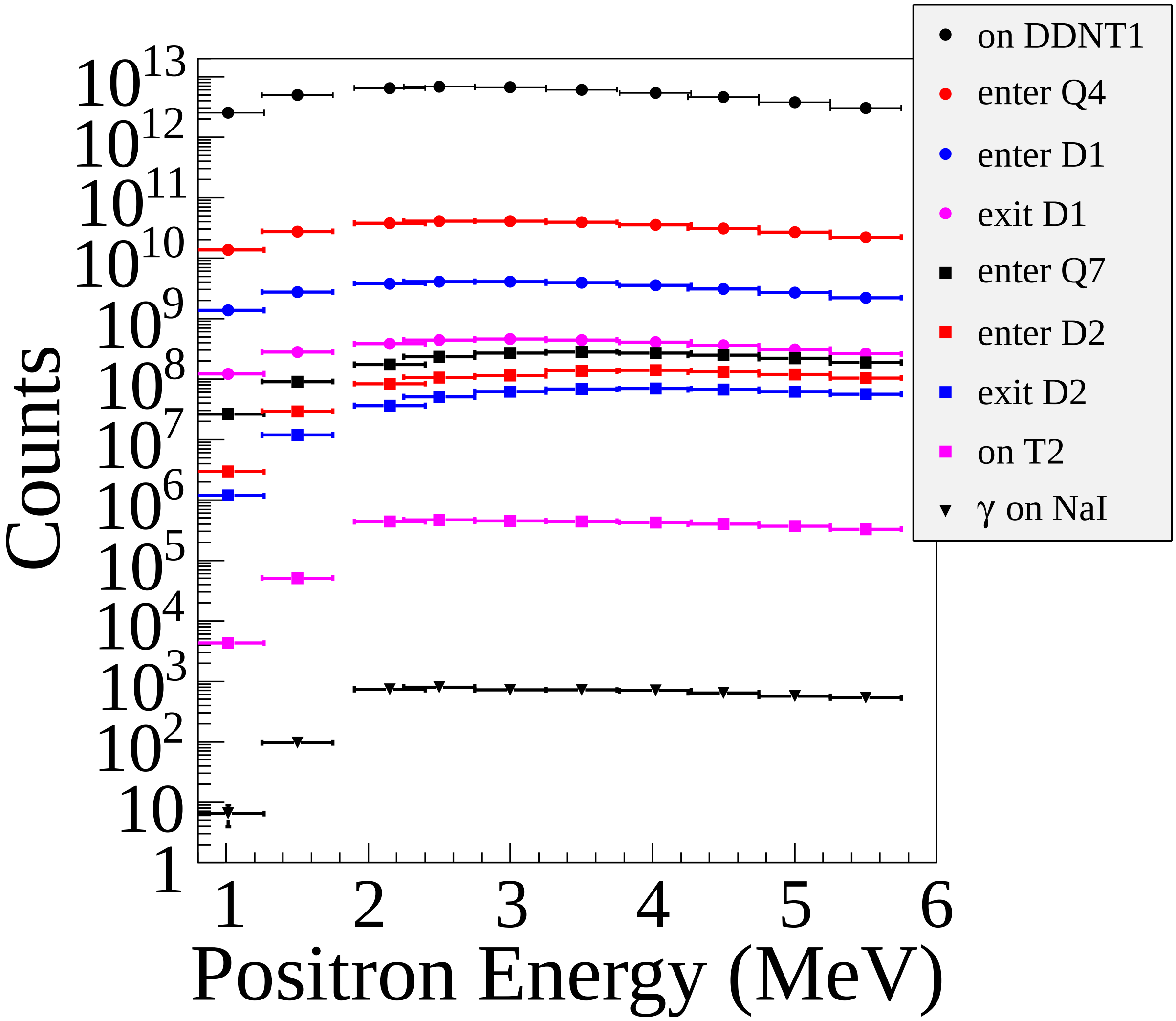

Figure 3.11: Predicted number positrons of transported. Black circle: positrons on DDNT1. Red circle: positrons enter Q4. Blue circle: positrons enter D1. Magenta circle: positrons exit D1. Black cube: positrons enter Q7. Red cube: positrons enter D2. Blue cube: positrons exit D2. Magenta cube: positrons on DT2UP. Black triangle: 511 keV photons detected by NaI detectors in coincidence mode.

two solid angles,$\Omega_{\mathrm{q4}}/\Omega_{\mathrm{beam}}$, is 1:160. That is to say 1 positrons in every 160 should make it from DDNT1 to the entrance of Q4, given the positrons beam is isotropic inside the cone. However, the positron beam peaks at smaller angle as shown in Fig. 3.3 (c) and (d). In the Fig. 3.12, dipoles are set to transport positrons with 3 MeV energy. 1.436×10^9 positrons (1/10 the on the Tab. 3.1) at the entrance of D1 are generated at the entrance of D1. Beam energy distribution is plotted at the exit of D1, entrance of Q7, exit of Q7, entrance of D2, exit of D2 and reach upstream T2 (not at T2, but at a virtual detector upstream of T2 with diameter as large as beam pipe inner diameter). During positron transportation, 4.1×10^8 enter and 4.6×10^7 exit D1, 2.7×10^7 enter and 2.5×10^7 exit Q7, 1.3×10^7 enter and 6.1×10^6 exit D2, and finally 1.2×10^5 reach the virtual detector few mm upstream of T2 (diameter of virtual detector is inner diameter of beam pipe).

The distance between NaI detectors and beamline center is 170 cm. The Pb shielding has a hole facing T2 with 2 inches diameter. Assuming positrons annihilated at center of T2, the solid angle NaI detector make is $\Omega = \frac{\pi r^2}{d^2} = \frac{\pi 25.4^2}{170^2}$. The 511 keV photons created during the annihilation are emitted isotropically, which makes an solid angle of 2π considering each side of T2 is facing one detector. The ratio of solid angle to the T2 makes to 2π is about 1:90. A simulation carried out using G4eamline that 10^5 5 MeV positrons incident on T2, created 43544 511 keV photons and 566 of them are detected on NaI detectors in coincidence. The ratio of the two is 84 which is close to the prediction from solid angle ratio. A 0.0254 mm thick stainless steel vacuum windows are placed 9 cm from T2 at two sides of beamline. Two detectors with 2 mm diameter placed at the two sides of the vacuum window to observe its affect on the photons (1 μm from the window). 1526 511 keV photons went into the vacuum window and 1514 make through without losing any energy. The loss is 0.8%.

3.4 Quadrupole Triplet Collection Efficiency Study

Quadrupole triplet positron collection and transportation efficiency was studied by regenerating positrons after T1. Several quadrupole current settings were simulated shown in

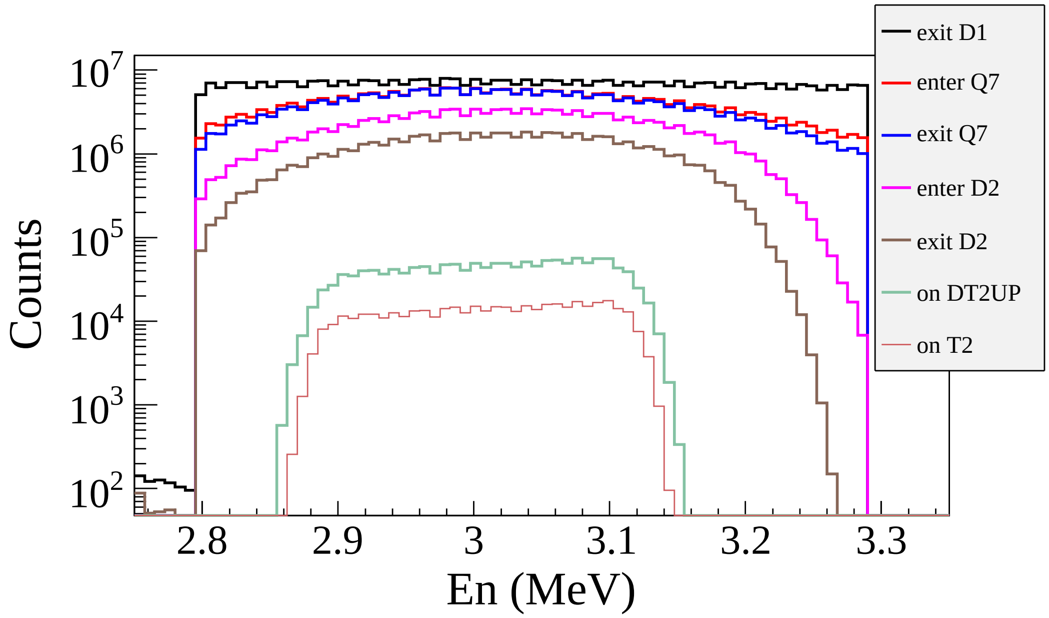

Figure 3.12: Beam transported when dipoles are set for 3 MeV positrons.

the Table. 3.2. 5,475,869,400 positrons generated and transported to the entrance of the D1, first dipole. A virtual detector is located at the entrance of the D1 to study collection and transportation efficiency of the triplet system. As it can be seen from the table, for different quadrupole settings, there are not any significant difference in number of positrons and their position and momentum distributions. On average, 3590413 positrons entered D1. The ratio of positrons generated to the ones enter D1 is 1525:1.

3.5 Error Study

Magnet settings are changed as shown Table. 3.3.The counts are given after considering the NaI detector efficiency in coincidence mode. In the table, Max/Min refer to the increase/decrease to the maximum/minimum possible the magnetic field of the magnets when the current of the dipole is changed by $\Delta \mathrm{I} = 0.1$ A. Def refers to the default magnetic field. The top 3 lines of the table is the magnet settings, and the counts are given corresponding columns below for the energies given in the left. The fractional error here is, $\frac{|\text{average } - \text{ defalt}|}{\text{defalt}}$

Table 3.2: Quadrupole Triplet System Collection and Transportation Efficiency Data.

Q4	Q5	Q6	Entries	x	σ_x	y	σ_y	P_x	σ_{P_x}	P_y	σ_{P_y}	P_z	σ_{P_z}
A	A	A		mm	mm	mm	mm	MeV	MeV	MeV	MeV	MeV	MeV
-1	2	-1	3587220	-0.005	12	0.030	12	3.0×10^{-5}	0.0461	-0.00216	0.04553	3.848	1.875
-2	4	-2	3591423	-0.012	12	0.049	12	2.2×10^{-5}	0.0461	-0.00211	0.04554	3.848	1.875
1	-2	1	3591509	-0.009	12	0.040	12	-1.5×10^{-5}	0.0462	-0.00216	0.04557	3.849	1.876
1	2	1	3589854	-0.005	12	0.034	12	-1.8×10^{-5}	0.0462	-0.00216	0.04556	3.849	1.876
2	-4	2	3592977	-0.007	12	0.032	12	-3.3×10^{-6}	0.0462	-0.00217	0.04549	3.849	1.876
2	4	2	3589495	-0.004	12	0.033	12	3.0×10^{-6}	0.0462	-0.00218	0.04554	3.849	1.875

in the counts.

Table 3.3: Systematic Error Study: Counts of NaI Detectors in Coincidence Mode for Different Magnet Settings.

D1	Max	Min	Max	Min	Max	Max	Min	Min	Def		
Q7	Def	Def	Def	Def	Max	Min	Min	Def	Def		
D2	Max	Min	Def	Def	Def	Def	Def	Def	Def		
Energy										Average	Fractional Error
0.77 - 1.27 MeV	12	6	1	3	5	1	1	2	6	4 ± 4	66.7%
1.25 - 1.75 MeV	78	72	72	77	66	89	75	60	78	74 ± 8	5.1%
1.85 - 2.35 MeV	591	580	581	576	535	630	588	535	583	578 ± 29	0.9%
2.25 - 2.75 MeV	635	610	607	602	616	611	616	625	572	610 ± 17	6.6%
2.75 - 3.25 MeV	597	604	605	593	586	632	589	573	577	595 ± 18	3.1%
3.25 - 3.75 MeV	579	588	586	589	575	582	553	553	565	574 ± 14	1.5%
3.77 - 4.27 MeV	562	491	566	563	553	564	559	550	564	552 ± 24	2.1%
4.25 - 4.75 MeV	525	520	523	520	508	525	514	511	530	520 ± 7	1.9%
4.75 - 5.25 MeV	469	4774	482	464	455	474	451	466	464	467 ± 10	0.6%
5.25 - 5.75 MeV	432	423	427	405	418	422	429	418	419	421 ± 8	0.5%

== Experiment ==

Chapter 4

Experiment

4.1 Quadrupole Scanning Experiment

The quadrupole current is changed to alter the strength and direction of the quadrupole magnetic field such that a measurable change in the beam shape is seen by the OTR system. Initially, the beam was steered by the quadrupole indicating that the beam was not entering along the quadrupole's central axis. Several magnetic elements upstream of this quadrupole were adjusted to align the incident electron beam with the quadrupole's central axis. First, the beam current observed by a Faraday cup located at the end of beam line was maximized using upstream steering coils within the linac nearest the gun. Second, the first solenoid nearest the linac gun was used to focus the electron beam on the OTR screen. Steering coils were adjusted to maximize the beam current to the Faraday cup and minimize the deflection of the beam by the solenoid first then by the quadrupole. A second solenoid and the last steering magnet shown in Fig 2.1, both near the exit of the linac, were used in the final step to optimize the beam spot size on the OTR target and maximize the Faraday cup current. A configuration was found that minimized the electron beam deflection when the quadrupole current was altered during the emittance measurements.

The emittance measurement was performed using an electron beam energy of 15 MeV and a 200 ns long, macro pulse of 40 mA current. The current in the first quadrupole after the exit of the linac was changed from − 5 A to + 5 A with an increment of 0.2 A. Seven measurements were taken at each current step in order to determine the average beam width and the variance. Background measurements were taken by turning the linac's electron gun off while keep the RF on. Background image and beam images before and after background subtraction are shown in Fig. 4.1. A small dark current is visible in Fig. 4.1 b that is known to be generated when electrons are pulled off the cavity wall and accelerated.

The electron beam energy was measured using a dipole magnet downstream of the quadrupole used for the emittance measurements. Prior to energizing the dipole, the electron micro-pulse bunch charge passing through the dipole was measured using a Faraday cup located approximately 50 cm downstream of the OTR screen. The dipole current was adjusted until a maximum beam current was observed on another Faraday cup located just after the 45 degree exit port of the dipole. A magnetic field map of the dipole indicates that the electron beam energy was 15 ± 1.6 MeV.

Images from the JAI camera were calibrated using the OTR target frame. An LED was used to illuminate the OTR aluminum frame that has a known inner diameter of 31.75 mm. Image processing software was used to inscribe a circle on the image to measure the circular OTR inner frame in units of pixels. The scaling factor can be obtained by dividing this length with the number of pixels observed. The result is a horizontal scaling factor of 0.04327 ± 0.00016 mm/pixel and vertical scaling factor of 0.04204 ± 0.00018 mm/pixel. Digital images from the JAI camera were extracted in a matrix format in order to take projections on both axes and perform a Gaussian fit. The observed image profiles were not well described by a single Gaussian distribution. The profiles may be described using a Lorentzian distribution, however, the rms of the Lorentzian function is not defined. A super Gaussian distribution was used [16], because rms values may be directly extracted. The Chi-square for x and y profiles are 2.4×10^7 and 1.9×10^7 for super Gaussian fit and 2.6×10^8 and 9.1×10^7 Gaussian fit. The beam spot, beam projections and fits are shown in Fig. 4.2. In Gaussian distribution, $\phi(x) = \frac{1}{\sqrt{2\pi}} e^{-\frac{1}{2}x^2}$, x on exponent is raised to the 2nd power. In the super Gaussian distribution, x on exponent is smaller than 2, resulting a sharper peak than Gaussian distribution. In Fig. 4.2 the super Gaussian fits raised x on exponent to $N_x = 0.9053$ and $N_y = 1.0427$.

Fig. 4.3 shows the square of the rms (σ_s^2) vs $k_1 L$ for x (horizontal) and y (vertical) beam projections along with the parabolic fits using Eq. 4.3. The emittance and Twiss parameters

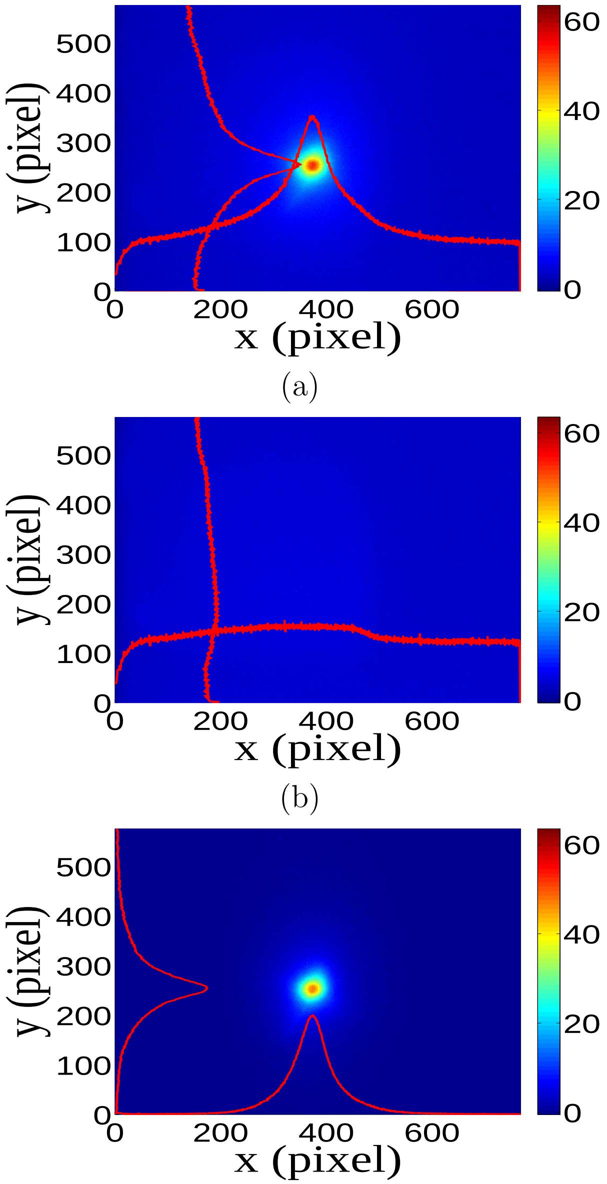

(a)

(b)

(c)

Figure 4.1: Digital image from the OTR screen; (a) a beam with the dark current and background noise, (b) a background image taken when RF is on gun is off, (c) a beam image when dark background was subtracted.

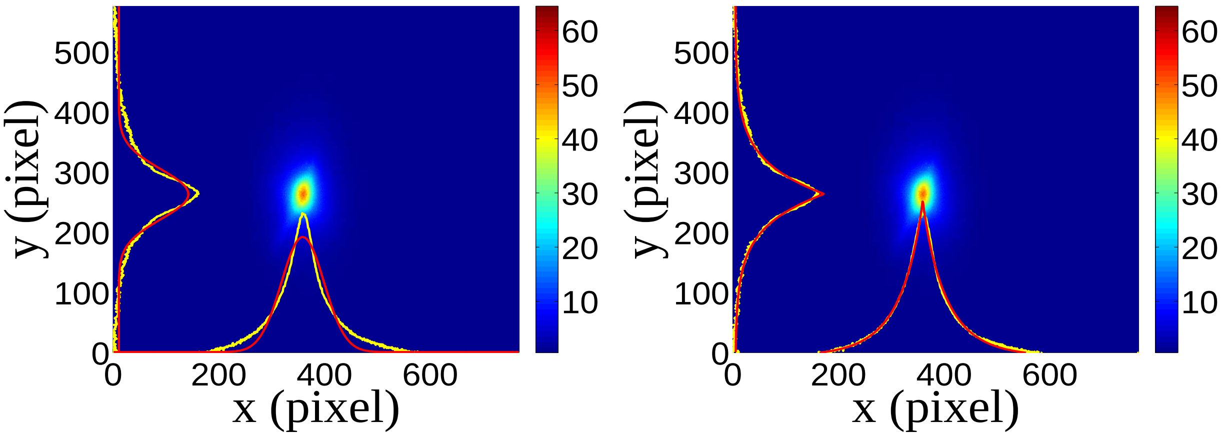

Figure 4.2: Gaussian and super Gaussian fits for beam projections. The beam images is background subtracted image and taken when quadrupole magnets are turned off. Left image is Gaussian fit and right image is super Gaussian fit.

from these fits are summarized in Table 4.1. MATLAB scripts used to calculate emittance and Twiss parameters are given in appendix B.

4.2 Energy Scan

An Energy scan was done to measure the energy profile of HRRL when it turned to accelerate electrons to 12 MeV peak energy. A Faraday cup was placed at the end of the 45 degree beamline to measure the electron beam current bent by the first dipole. Dipole coil current was changed in 1 A increments and the Faraday cup current was recorded. The relation between dipole current and beam energy is given in the appendix A. As shown in Fig. 4.4 A 12 MeV peak observed with long low energy tail. The energy distribution of HRRL can be described by two skewed Gaussian fits overlapping [16]. The skewed Gaussian fit function is given as,

$$G(En) = A_1 e^{-\frac{-(En-\mu_1)^2}{2(\sigma_1(1+sign(En-\mu_1))E_1)^2}} + A_2 e^{-\frac{-(En-\mu_2)^2}{2(\sigma_2(1+sign(En-\mu_2))E_2)^2}} \tag{4.1}$$

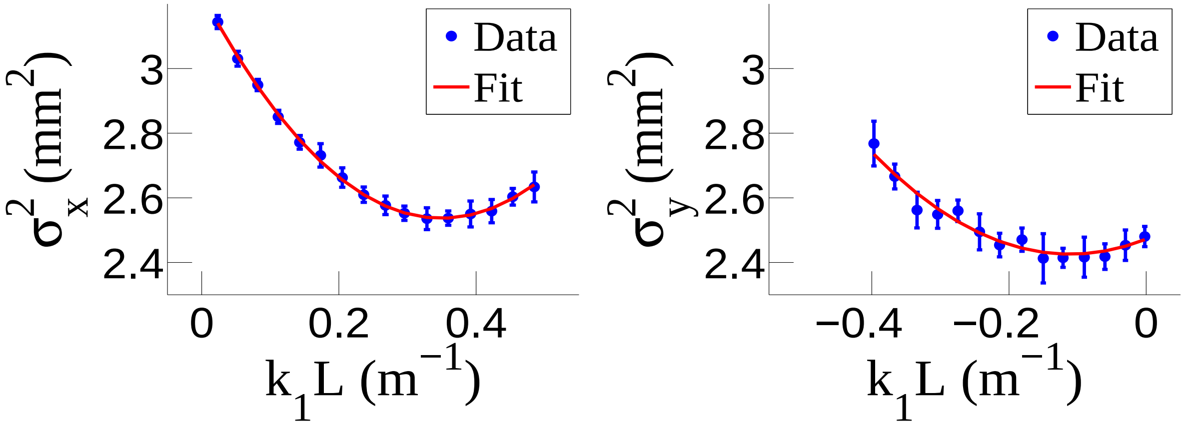

Figure 4.3: Square of rms values and parabolic fittings.

Table 4.1: Emittance Measurement Results

Parameter	Unit	Value
projected emittance ϵ_x	μm	0.37 ± 0.02
projected emittance ϵ_y	μm	0.30 ± 0.04
β_x-function	m	1.40 ± 0.06
β_y-function	m	1.17 ± 0.13
α_x-function	rad	0.97 ± 0.06
α_y-function	rad	0.24 ± 0.07
micro-pulse charge	pC	11
micro-pulse length	ps	35
energy of the beam E	MeV	15 ± 1.6
relative energy spread $\Delta E/E$	%	10.4

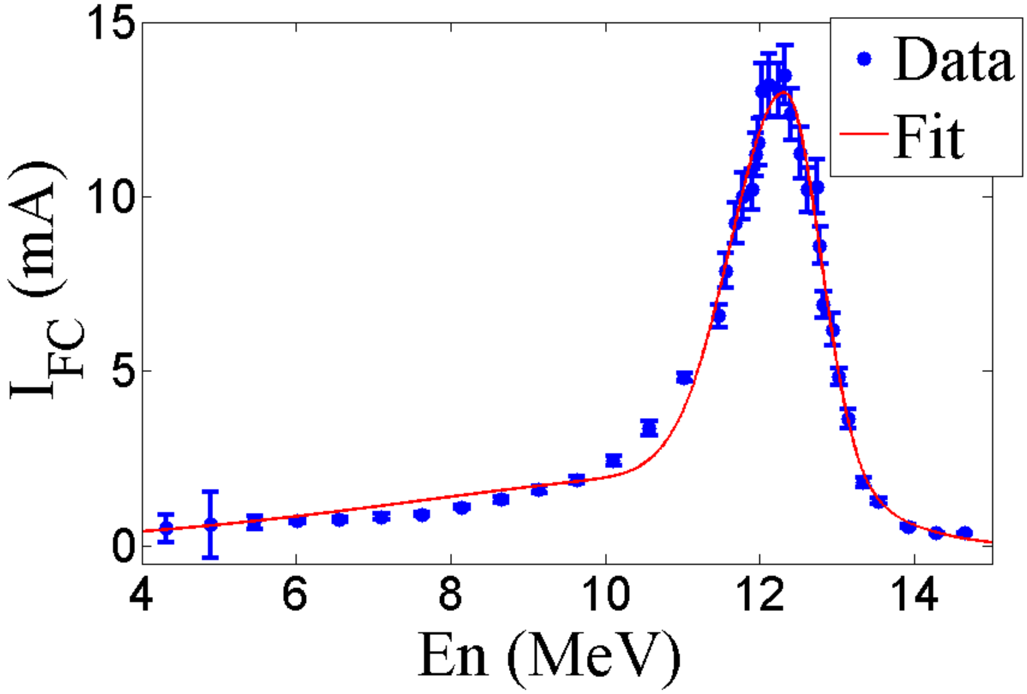

Figure 4.4: HRRL energy scan (blue dots) and fit (red line) with two skewed Gaussian distribution.

where, $\sigma_1 = \frac{\sigma_{r,1}+\sigma_{l,1}}{2}$, $\sigma_2 = \frac{\sigma_{r,2}+\sigma_{l,2}}{2}$, $E_1 = \frac{\sigma_{r,1}-\sigma_{l,1}}{\sigma_{r,1}+\sigma_{l,1}}$, and $E_2 = \frac{\sigma_{r,2}-\sigma_{l,2}}{\sigma_{r,2}+\sigma_{l,2}}$. The measurement result and fit are shown in Fig. 4.4 and in Table 4.2.

4.3 Positron Production Runs

The annihilation target T2 is can be inserted or removed from the center of the beamline. This allow two kind runs, T2 in and T2 out. When T2 is in the positions are delivered to

Table 4.2: Two Skewed Gaussian Parameters Describes Energy Distribution.

Parameter	Unit	First Gaussian	Second Gaussian
amplitude A	mA	2.14	10.88
mean μ	MeV	12.07	12.32
sigma left σ_L	MeV	4.47	0.70
sigma right σ_R	MeV	1.20	0.45

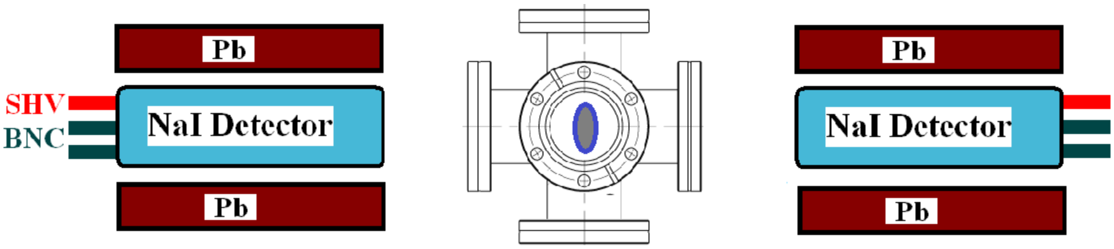

Figure 4.5: Positron detection using T2 and NaI detectors.

Table 4.3: Run Parameters of Run No. 3735.

Parameter	Unit	Value
run number		3735
repetition rate	Hz	300
run time	s	1002
pulses		301462
events		9045
e+ Counts NaI Detectors		256 ± 16

T2 and thermalize and annihilate produces 511 keV photons. This photons are detected by the NaI detectors as shown in Fig. 4.5. When T2 is out, positrons exits beamline and transported to the beam dump. NaI detectors are shielded with Pb bricks from the beam dump. T2 out runs serve as background measurements.

T2 is placed inside a 6-way cross and two horizontal side it sealed with thin windows. Two NaI detectors placed horizontally to T2, perpendicular to the 90 degree beamline and pointed to this windows. The spectrum taken with T2 in and out are shown in the Fig. 4.6.

Run No. 3735 (T2 in) and run No. 3736 (T2 out) in the Fig. 4.6, the two sub-figures acquired by cut that only incidents happened in 511 keV peak coincidently on both detectors. The positron counts extracted by subtracting background (blue in figure) and integrating the peak. The integral shown in red is from the background is subtracted spectrum. The run parameters of Run No. 3735 is given in Table. 4.3

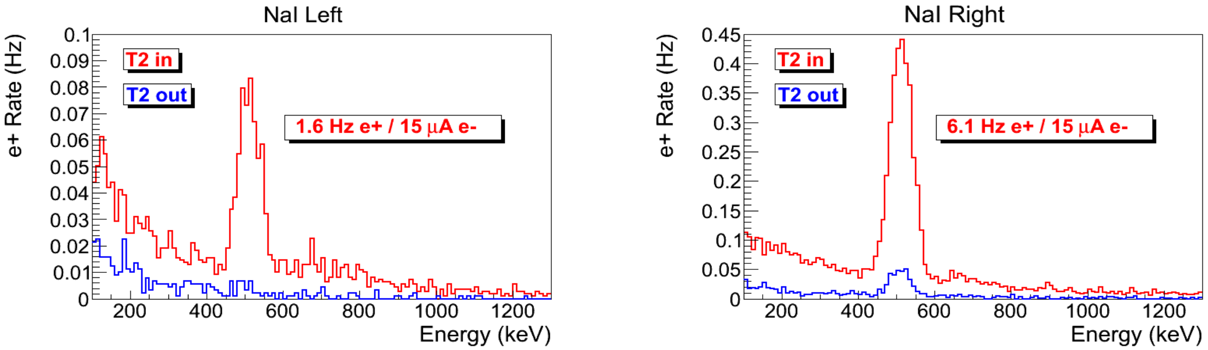

(a) Original spectrum on left NaI.

(b) Original spectrum on right NaI.

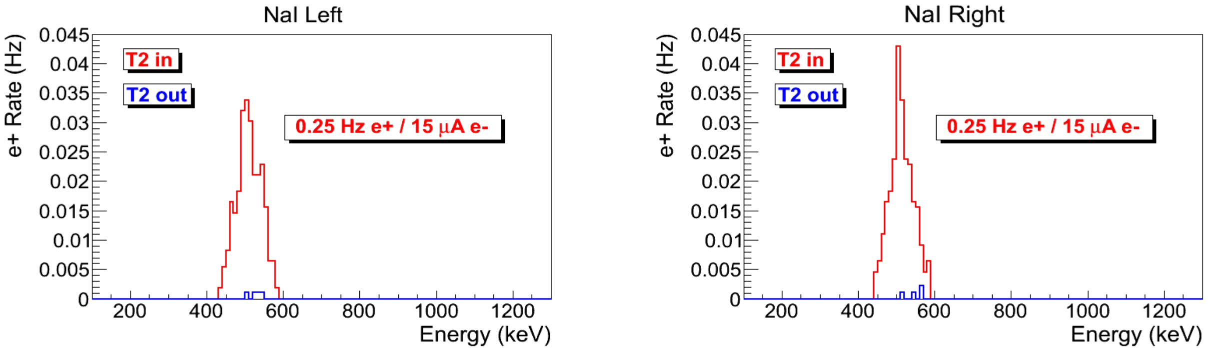

(c) Spectrum with cut on left NaI.

(d) Spectrum with cut on right NaI.

Figure 4.6: T2 in run (red) and T2 out background run (blue) time normalized spectrum. Top row shows original spectrum and bottom row shows incidents only happen in 511 keV peak coincidently on both detectors.

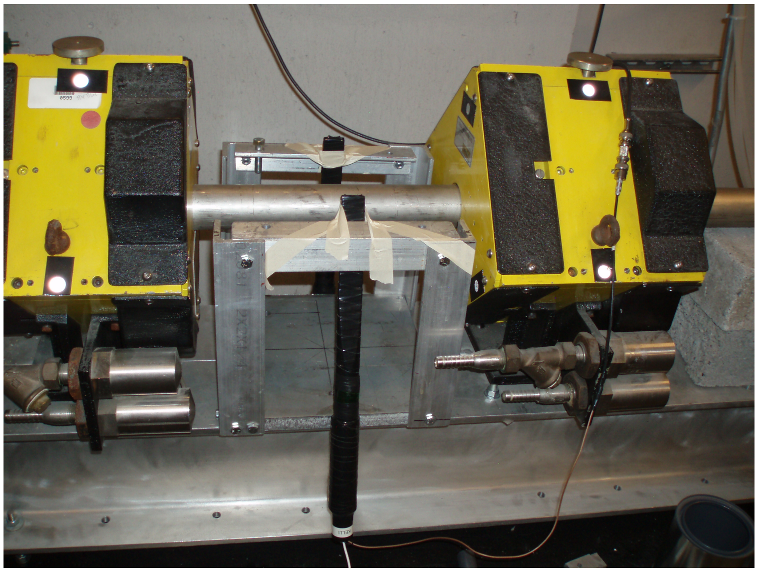

Figure 4.7: Electron beam monitor.

Table 4.4: Scintillator Calibration Data.

Run Number	Faraday Cup Charge Area (nVs)	Mean of ADC Channel 9
3703	1201 ± 10	1126 ± 0.8
3705	777 ± 110	791.8 ± 0.6
3706	367.7 ± 2.3	242.1 ± 0.3

4.4 Electron Current Estimation

A photon scintillator was placed between quadrupole 9 and quarupole 10 shown as in the Fig. 4.7 and used as electron beam monitor. To calibrate this scintillator electron beam changed incrementally and the charge was measured both on oscilloscope and ADC. As the electron beam increases the beam charge observed on the scope increased and the photon peak in the ADC also shifted towards right end of the spectrum. The measured results are shown in the Table 4.4. The result shows that the relation between electron beam current and scintillator ADC channel number is linear, $(0.93 \pm 0.14)/50$ nVs/(ADC channel number). The spectrum taken is shown in Fig 4.8.

To find the average charge in a run two methods were used. One method calculates

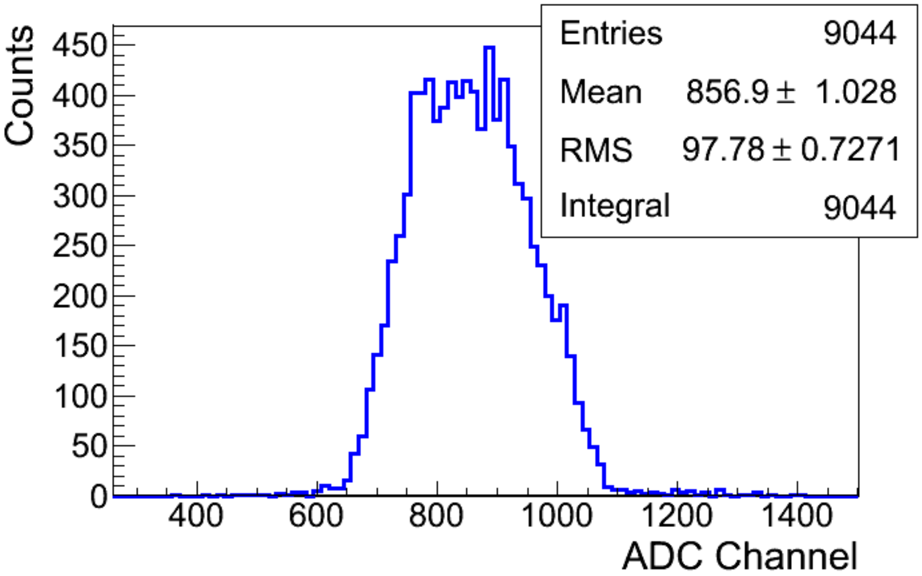

Figure 4.8: Electron beam monitor ADC signal

charge bin by bin and add up charges in all the bins as shown in Eq. 4.2

$$Q_{e^-} = \sum_i i \times (bin\ content[i]) \times Q_{Calb} \times (pulses/events). \tag{4.2}$$

In another method, the mean of the of the spectrum multiplied with total number of pulses in the run as shown in Eq. 4.3. Of course the calibration factors multiplied in both methods. The average of the two methods is taken.

$$Q_{e^-} = (Mean\ ADC\ Channel\ Number) \times (pulses) \times Q_{Calb}. \tag{4.3}$$

The average of the two in run 3735 is $(4.8 \pm 0.5) \times 10^{-3}\ C$. Then this total charge can be used to calculate total numbers of the electrons or average current of electron beam in this run.

Table 4.5: Run 3735

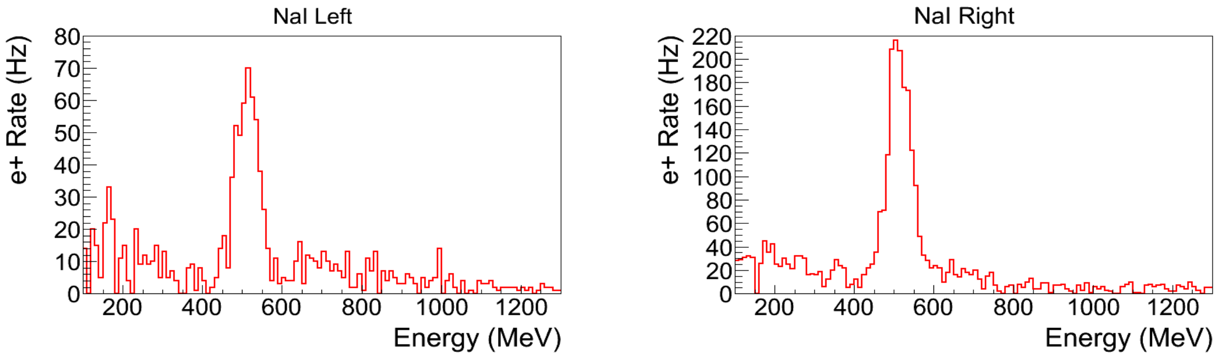

(a) Left NaI

(b) Right NaI

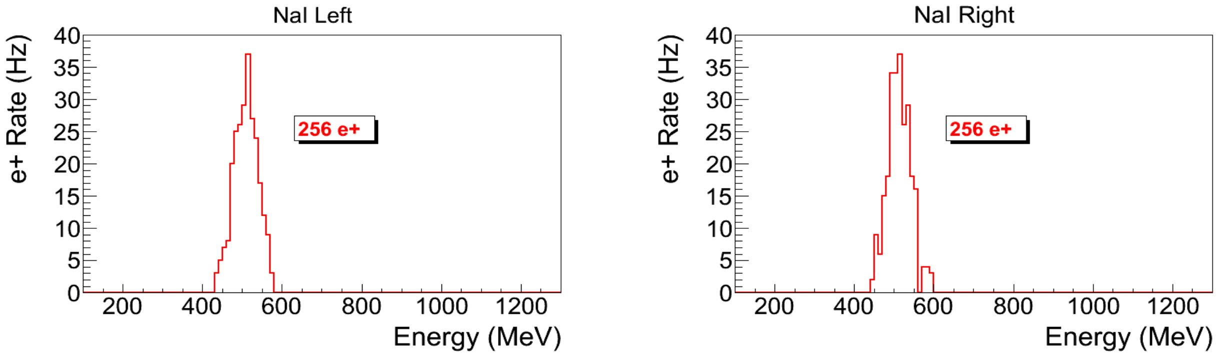

(c) Left NaI with cut and coincidence

(d) Right NaI with cut and coincidence

Table 4.6: NaI positron run spectrum.

4.5 Positron Rate Estimation

Fig. 4.5 are the background subtracted spectrum. The (a) and (b) are NaI left and right detectors' spectrum. The (c) and (d) are NaI left and right detectors' spectrum with cut around 511 keV peak and after requiring coincident event on both detectors.

The measured ratio of positron to electron ratio is given the following Table 4.7 and Fig. 4.9.

To find Error on the energy, the 3 MeV electron beam is directed to the phosphorous screen at the end of the 90 degree beamline. The beam centered then steering away from

Table 4.7: Positron to Electron Rate Ratio.

Energy	Positron to Electron Ratio
1.02 ± 0.06	$(0.19 \pm 0.19) \times 10^{-16}$
2.15 ± 0.06	$(0.69 \pm 0.24) \times 10^{-16}$
3.00 ± 0.06	$(8.25 \pm 0.96) \times 10^{-15}$
4.02 ± 0.06	$(4.20 \pm 0.80) \times 10^{-15}$
5.00 ± 0.06	$(0.62 \pm 0.16) \times 10^{-16}$

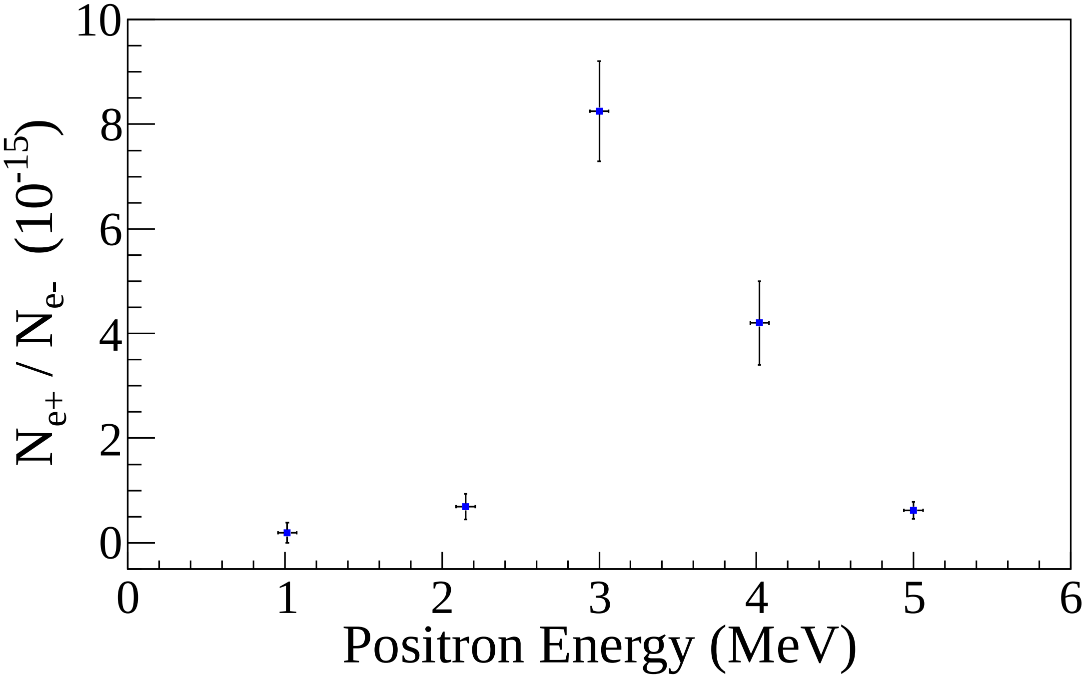

Figure 4.9: Ratio of positrons detected to electrons in experiment.

the center by changing the current by $\Delta I = 0.1$ A. This 0.1 A change in the dipole current corresponding to 0.06 MeV differece in the beam energy for 3 MeV beam. For other energies, the it is also 0.06 MeV after rounding up.

= Conclusions and Suggestions =

Chapter 5

Conclusions and Suggestions

1. HRRL beamline: The HRRL cavity placed to new location. New magnetic elements and diagnostic tolls added to the beamline. HRRL beam successfully reconfigured for positron production and can also generate electron beam with improved quality.

2. A diagnostic tool was developed and used to measure the beam emittance of the High Rep Rate Linac at the Idaho Accelerator Center. The tool relied on measuring the images generated by the optical transition radiation of the electron beam on a polished thin aluminum target. The electron beam profile was not described well using a single Gaussian distribution but rather by a super Gaussian or Lorentzian distribution. The larger uncertainties observed for σ_y^2 are still under investigation. The projected emittance of the High Repetition Rate Linac, similar to medical linacs, at ISU was measured to be less than 0.4 μm as measured by the OTR based tool described above when accelerating electrons to an energy of 15 MeV.

3. Successfully constructed a positron detection system using two NaI detectors, thin tungsten foils a 6-way cross.

4. Successfully measured positrons at different energies ($1 - 5$ MeV) in experiment. The ratio of positrons being detected on NaI detectors to electrons incident on T2 is on the order of 10^{-15} and peak distribution observed around 3 MeV.

5. In the experiment quarupoles were optimized to transport 2 MeV due to the limited beam time and it could have diminished transportation efficiency for other energies. Further experimental study is necessary to investigate the positron beam energy distribution.

6. Simulation results indicate that the transportation efficiency are varies for different energies. Higher energies has better transportation efficiency. While simulation results

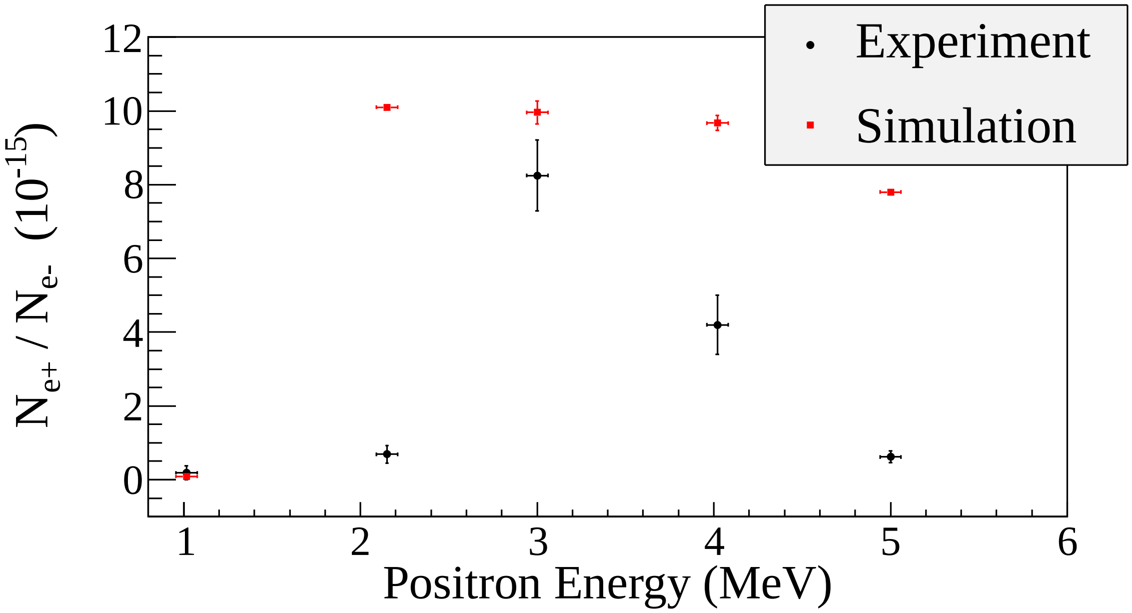

Figure 5.1: Ratio of positrons detected to electrons in experiment and simulation.

agrees with experiment in the peak energy distribution is around 3 MeV, it disagrees with experiment in the ratio of the peak to other energies.

7. Experimental results show quarupole magnet is not efficient in collecting positrons, since positrons have large angular distribution. Solenoid can be used to improve the collection efficiency of positrons [17] and should be placed as close the production target as possible for better efficiency.

Appendix A

Electron Beam Energy Scan

Electron beam energy was scanned using dipole magnet. The dipole magnet was set to bend electron beam with certain energy. The beam current corresponding to that bent electron beam energy was observed on a Faraday cup and oscilloscope.

Table A.1: Dipole Magnet Mapping Data.

Dipole Magnet Coil Current (A)	**Faraday Cup Current (mA)**	**Electron Beam Energy (MeV)**
8	0.5	4.3119
9	0.6	4.8896
10	0.67	5.4570
11	0.716	6.0141
12	0.752	6.5610
13	0.828	7.0975
14	0.896	7.6238
15	1.112	8.1399
16	1.328	8.6456
17	1.624	9.1411
18	1.896	9.6262
19	2.448	10.1012
20	3.36	10.5658

Continued on next page

Table A.1 – *Continued from previous page*

Dipole Magnet Coil Current (A)	**Faraday Cup Current (mA)**	**Electron Beam Energy (MeV)**
21	4.82	11.0201
22	6.58	11.4642
22.2	7.88	11.5518
22.5	9.24	11.6824
22.7	10.0	11.7690
23	10.2	11.8980
23.1	11.2	11.9408
23.2	11.56	11.9836
23.3	13.04	12.0262
23.5	13.2	12.1111
23.8	13.04	12.2377
24	13.48	12.3216
24.2	12.36	12.4050
24.5	11.24	12.5295
24.7	10.2	12.6119
25	10.28	12.7348
25.1	8.6	12.7756
25.2	6.92	12.8162
25.5	6.2	12.9376
25.7	4.84	13.0180
26	3.64	13.1378
26.5	1.82	13.3354
27	1.28	13.5305

Continued on next page

Table A.1 – *Continued from previous page*

Dipole Magnet Coil Current (A)	**Faraday Cup Current (mA)**	**Electron Beam Energy (MeV)**
28	0.56	13.9129
29	0.364	14.2850
30	0.364	14.6469

Appendix B

MATLAB Scripts for Calculating Emittance

The main script

`"Emit_Calc.m`

loads and digitize electron beam images. By projecting the 2D beam to the axis, 1D beam profile is extracted and passed to

`SupGau_devsum.m`

for super Gaussian fitting.

`SupGau_devsum.m`

returns rms of the super Gaussian fit. The rms values of different images are sent to

`Emit_Parabola_Fit_kl_XProjection`

.

`Emit_Parabola_Fit_kl_XProjection`

fits parabola for given rms values, plots the fit and extract emittance from the fit.

B.1 Emittance Calculator

```
% Emit_Calc.m
% Reads images from files and digitize images.
% Fits a super Gaussian funtion on the projection, get the rms values.
% Then pass them to fit parabola
%
% April-2011
% Sadiq Setiniyaz

clc;
clear

me = 0.511; % electron rest mass in MeV
%En = 14; %enter beam energy here in MeV unit.
En = 14.9985 ; %14.9985 MeV energy at Mar 17th, 2011.
En_er = En*0.1; % Assume 5% error on Energy
L = 0.08; % pole face is 8 cm long in z direction.
R_Bore = 0.0254; %Radius of the Bore aperture = center to pole face = 1 inch.
%L_ef = L + R_Bore;
%I_max_neg = -10; %enter smallest negative scan current. Here -7 Amps
%I_max_pos = 7; %enter biggest positive scan current. Here 10 Amps
I_start=-3.0; % Scan starting current
%I_end=-2.0; % Scan ending current
I_increment=0.2;
scan_current_number=31; % do 13 scan.
scan_times=7;
```

```
%for ii = 1:scan_step
%    I(ii) = I_start + (ii-1)*I_increment;
%end

p = sqrt(En*En - me*me)/1000;% e- momentum in GeV/c

%%%%%%%%%%%%%%%%%%%%%%%%%%%%%%%%%%%%%%%%%%%%%
% Enter the distance from the center of the quad to the screen
S12=3.1;%(in m unit) S12(q4)=1.875 cm. S12(q1)=3.10 cm
erS12 = 0.005; % assume 51 mm error.
%%%%%%%%%%%%%%%%%%%%%%%%%%%%%%%%%%%%%%%%%%%%%

%%%%%%%%%%%%%%%%%%%%%%%%%%%%%%%%%%%%%%%%%%%%%%%%%%%%%%%%%%%%
%Enter calibration here:
calibration_x=0.04327*0.001; %m/px
calibration_y=0.04204*0.001; %m/px
er_calibration_x=0.00016*0.001;
er_calibration_y=0.00018*0.001;
%%%%%%%%%%%%%%%%%%%%%%%%%%%%%%%%%%%%%%%%%%%%%%%%%%%%%%%%%%%%

disp('Reading image ...')
% Get image for background. For background RF is on, gun is off.

bg1 = imread('Scan_1\RF_on_Gun_off_bg.bmp');
bg2 = imread('Scan_2\RF_on_Gun_off_bg.bmp');
bg3 = imread('Scan_3\RF_on_Gun_off_bg.bmp');
bg4 = imread('Scan_4\RF_on_Gun_off_bg.bmp');
```

```
bg5 = imread('Scan_5\RF_on_Gun_off_bg.bmp');
bg6 = imread('Scan_6\RF_on_Gun_off_bg.bmp');
bg7 = imread('Scan_7\RF_on_Gun_off_bg.bmp');
% Averaging background.
bg = (bg1+bg2+bg3+bg4+bg5+bg6+bg7+bg7+bg7)/7;
imd_bg = double(bg(:,:,1));

for ii=1:scan_times
switch ii
    case 1
        addpath(genpath('\Scan_1'));
    case 2
        addpath(genpath('\Scan_2'));
    case 3
        addpath(genpath('\Scan_3'));
    case 4
        addpath(genpath('\Scan_4'));
    case 5
        addpath(genpath('\Scan_5'));
    case 6
        addpath(genpath('\Scan_6'));
    case 7
        addpath(genpath('\Scan_7'));
end

% Read OTR images.
for scan = 1:scan_current_number;
    thisfilename=ii;
```

```
    imNo = ii;
    I(scan) = I_start + (scan-1)*I_increment;
    switch scan
       case 1
% Devide the effetive length by 100 to convert to meter unit.
            im = imread('negative\11.bmp');
            tifname='11';
            L_ef(scan) = 9.95/100;
            Er_L_ef(scan) = 0.17/100;
        case 2
            im = imread('negative\12.bmp'); % reading 1.png
            tifname='12';
            L_ef(scan) = 9.91/100;
            Er_L_ef(scan) = 0.16/100;
        case 3
            im = imread('negative\13.bmp');
            tifname='13';
            L_ef(scan) = 9.91/100;
            Er_L_ef(scan) = 0.16/100;
        case 4
            im = imread('negative\14.bmp');
            tifname='14';
            L_ef(scan) = 9.85/100;
            Er_L_ef(scan) = 0.14/100;
        case 5
            im = imread('negative\15.bmp');
            tifname='15';
            L_ef(scan) = 9.85/100;
```

```
            Er_L_ef(scan) = 0.16/100;
        case 6
            im = imread('negative\16.bmp');
            tifname='16';
            L_ef(scan) = 9.87/100;
            Er_L_ef(scan) = 0.19/100;
        case 7
            im = imread('negative\17.bmp');
            tifname='17';
            L_ef(scan) = 9.82/100;
            Er_L_ef(scan) = 0.19/100;
        case 8
            im = imread('negative\18.bmp');
            tifname='18';
            L_ef(scan) = 9.86/100;
            Er_L_ef(scan) = 0.17/100;
    end
    sg = im; % reading 1.png
imd_sg = double(sg(:,:,1));
pic = (imd_sg-imd_bg);
%imd = imd_sg;
%imd = imd_bg;

% Noise Cleaning.
% Getting red of the dead pixels.
% If there is sudden increase in the pixel brightness,
% Then use the pixel brightnesss of the earlier pixel.
for i = 3:768
```

```
for j = 3:576
    if pic(j,i)>500
       pic(j,i)=pic(j-1,i);
    elseif pic(j,i)-pic(j-2,i)>20
            pic(j,i)=pic(j-1,i);
    end
end
end

% Determine image size in pixels.
dim=size(pic);
%dim=size(imd);
dim_x = dim(1);
dim_y = dim(2);

xunit='m';
yunit='m';

% Beam transverse profiles.
profx = sum(pic,1); % make x projection
profy = sum(pic,2)';% make y projection

xbins=size(profx);
ybins=size(profy);
x=(1:1:xbins(2));
y=(1:1:ybins(2));

% Set Gaussian fit range.
```

```
xl = 1;
xr = 766;
yl = 1;
yr = 576;

% Checking.
%plot(x,profx,'k');
%hold on;
%plot(y,profy,'k');
%hold on;

% Initialize fit parameters.
% a1= base. a2 = A; amplitude. a3 = mean. a4 = D; sigma_0. a5 = N;
a1 = 100;
a2 = 7700;
a3 = 280;
a4 = 39;
a5 = 1;

% SupGau = a(1)+a(2)*exp(-abs(X-a(3))/(a(4))).^a(5); % super gaussian.
% Putting the parameters together.
a0 = [a1,a2,a3,a4,a5];
% Setting fit criteria and use fminsearch optimization.
opts = optimset('TolX',1e-4,'MaxFunEvals',10000,'MaxIter',10000,'Display','on');
% Pass fit parameters to SupGau_devsum.
[fitpara_x,fval_x,flag_x,err_x] = fminsearch(@SupGau_devsum,a0,opts,x,profx);
[fitpara_y,fval_y,flag_y,err_y] = fminsearch(@SupGau_devsum,a0,opts,y,profy);
% Get the fit parameters of x profile.
```

```
base_x = fitpara_x(1);
amplitude_x = fitpara_x(2);
peak_center_x = fitpara_x(3);
sig0_x = fitpara_x(4);
N_x = fitpara_x(5);
sig_x(scan,imNo) = sig0_x*(pi/2).^(2/fitpara_x(5)-1);
% Get the fit parameters of y profile
base_y = fitpara_y(1);
amplitude_y = fitpara_y(2);
peak_center_y = fitpara_y(3);
sig0_y = fitpara_y(4);
N_y = fitpara_y(5);
sig_y(scan,imNo) = sig0_y*(pi/2).^(2/fitpara_y(5)-1);

% Printing out parameters to check.
string_x = [
    num2str(I(scan),'  %2.2f'),'    ', ...
    num2str(imNo,'%d'),'      ', ...
    num2str(base_x,'%12.2f'),'      ', ...
    num2str(amplitude_x,'%12.f'),'         ', ...
    num2str(peak_center_x,'%12.2f'),'      ', ...
    num2str(N_x,'%12.4f'),'    ', ...
    num2str(sig0_x,'%12.2f'),'      ', ...
    num2str(sig_x(scan,imNo),'%12.2f'),'    ', ...
    ];
%disp(string_x);
string_y = [
    num2str(I(scan),'  %2.2f'),'    ', ...
```

```
    num2str(imNo,'%d'),'      ', ...
    num2str(base_y,'%12.2f'),'      ', ...
    num2str(amplitude_y,'%12.f'),'         ', ...
    num2str(peak_center_y,'%12.2f'),'      ', ...
    num2str(N_y,'%12.4f'),'    ', ...
    num2str(sig0_y,'%12.2f'),'      ', ...
    num2str(sig_y(scan,imNo),'%12.2f'),'    ', ...
    ];
%disp(string_y);
%sig

% Plot to check.
%plot(x,profx,'k');
%hold on;
%plot(y,profy,'k');
%hold on;


% Construct fit curve from the fit parameters.
y_fit_x = fitpara_x(1)+fitpara_x(2)*exp( -0.5*(abs(x-fitpara_x(3))/
(fitpara_x(4))).^fitpara_x(5) );
y_fit_y = fitpara_y(1)+fitpara_y(2)*exp( -0.5*(abs(y-fitpara_y(3))/
(fitpara_y(4))).^fitpara_y(5) );

%plot(x,y_fit_x,'r');

%plot(y,y_fit_y,'r');
drawnow
```

```
end
end

for scan=1:scan_current_number

% Find mean and standar deviation.
sig_mean_x(scan) = mean(sig_x(scan,:));
sig_mean_y(scan) = mean(sig_y(scan,:));
sig_x_er(scan)   = std(sig_x(scan,:));
sig_y_er(scan)   = std(sig_y(scan,:));

% Converting from pixels to length (in m unit).
sig_mean_x(scan)=sig_mean_x(scan)*calibration_x; %
sig_mean_y(scan)=sig_mean_y(scan)*calibration_y; %
sig_x_er(scan)= sqrt((sig_x_er(scan)*calibration_x).^2+(sig_mean_x(scan)*
er_calibration_x).^2);
sig_y_er(scan)= sqrt((sig_y_er(scan)*calibration_y).^2+(sig_mean_y(scan)*
er_calibration_y).^2);

% Squared sigma.
sig_sqr_x(scan) = sig_mean_x(scan)*sig_mean_x(scan);
sig_sqr_x_er(scan) = 2*sig_mean_x(scan)*sig_x_er(scan);
sig_sqr_y(scan) = sig_mean_y(scan)*sig_mean_y(scan);
sig_sqr_y_er(scan) = 2*sig_mean_y(scan)*sig_y_er(scan);



%I(scan) = I_start + (scan-1)*I_increment;
%plot(I,sig_mean,'r');
```

```
%Get the quarupole strength and its error from the dipole current.
k1(scan) =0.2998*(3.6*0.0001+1945*0.000001*I(scan))/(0.0254*p);

k1_Er(1) =0.2998*((3.6+1.3)*0.0001+(1945+2)*0.000001*I(scan))/(0.0254*p);
k1_Er(2) =0.2998*((3.6-1.3)*0.0001+(1945+2)*0.000001*I(scan))/(0.0254*p);
k1_Er(3) =0.2998*((3.6+1.3)*0.0001+(1945-2)*0.000001*I(scan))/(0.0254*p);
k1_Er(4) =0.2998*((3.6-1.3)*0.0001+(1945-2)*0.000001*I(scan))/(0.0254*p);
er_k1(1)=abs(k1(scan)-k1_Er(1));
er_k1(2)=abs(k1(scan)-k1_Er(2));
er_k1(3)=abs(k1(scan)-k1_Er(3));
er_k1(4)=abs(k1(scan)-k1_Er(4));

k1_er(scan)=max(er_k1);

k1L(scan) = L_ef(scan)*k1(scan); %k1*L
er_k1L(scan) = sqrt((L_ef(scan)*k1_er(scan) )^2+(Er_L_ef(scan)*k1(scan))^2);
%er_k1L(scan) = L_ef*k1_er(scan);

% Put the parameters together to pass to parabolic fits
FitDatX = [k1L’,er_k1L’,sig_sqr_x’,sig_sqr_x_er’];
FitDatY = [k1L’,er_k1L’,sig_sqr_y’,sig_sqr_y_er’];

end

 X_fit_data = fopen(’X_fit_data.txt’,’w’);
 Y_fit_data = fopen(’Y_fit_data.txt’,’w’);
 %fprintf(X_fit_data,’%4f %4f %4f %4f \n’,k1L(16:31)’,er_k1L(16:31)’,
 sig_sqr_x(16:31)*10^6’,sig_sqr_x_er(16:31)*10^6’);
```

```
 %fprintf(Y_fit_data,'%4f %4f %4f %4f \n',k1L(2:15)',er_k1L(2:15)',
 sig_sqr_y(2:15)*10^6', sig_sqr_y_er(2:15)*10^6');
 fprintf(X_fit_data,'%4f %4f %4f \n',k1L(16:31)', sig_sqr_x(16:31)'*10^6,
 sig_sqr_x_er(16:31)'*10^6);
 fprintf(Y_fit_data,'%4f %4f %4f \n',k1L(2:15)', sig_sqr_y(2:15)'*10^6,
 sig_sqr_y_er(2:15)'*10^6);
 fclose(X_fit_data);
 fclose(Y_fit_data);

% Converting to cgs (mm and mrad) units.
 [k1L(16:31)' sig_sqr_x(16:31)'*10^6 sig_sqr_x_er(16:31)'*10^6]
 [k1L(2:15)' sig_sqr_y(2:15)'*10^6 sig_sqr_y_er(2:15)'*10^6]

%Emit_Parabola_Fit_kl_XProjection(k1L,er_k1L,sig_sqr_x,sig_sqr_x_er,me,En,
S12,erS12,scan_current_number);
%Emit_Parabola_Fit_kl_YProjection(k1L,er_k1L,sig_sqr_y,sig_sqr_y_er,me,En,
S12,erS12,scan_current_number);
Emit_Parabola_Fit_kl_XProjection(k1L(16:31),er_k1L(16:31),
sig_sqr_x(16:31)*10^6,sig_sqr_x_er(16:31)*10^6,me,En,En_er,S12,erS12,16);
Emit_Parabola_Fit_kl_YProjection(k1L(2:15) ,er_k1L(2:15),
sig_sqr_y(2:15)*10^6, sig_sqr_y_er(2:15)*10^6, me,En,En_er,S12,erS12,14);
```

B.2 Super Gaussian Fit

`SupGau_devsum.m`

function is being called during by

`Emit_Calc.m`

to fit super Gaussian to beam transverse profile.

```
function chisq = SupGau_devsum(a,X,Y)
% a(1) = base
% a(2) = A;  %amplitude
% a(3) = x0; %center
% a(4) = D;  %sigma_0
% a(5) = N;  %N=2 is nomal Guassian.
             %N<super Gaussian (sharp top).
             %N>Flat top shape Gaussian.
SupGau = a(1)+a(2)*exp( -0.5*(abs(X-a(3))/(a(4))).^a(5) ); % super Gaussian
csq = (Y - SupGau).^2;
chisq = sum(csq);
return
```

B.3 Parabolic Fit

`Emit_Parabola_Fit_kl_XProjection`

fits parabola for given rms values, plots the fit and extract emittance from the fit.

```
function varargout = Emit_Parabola_Fit_kl_XProjection(x,erx,y,ery,me,En,
En_er,S12,erS12,NumPoints)


%x
%y
%ery


order = 2; % second order fit
ParNum = order + 1;
```

```
% finding row matrix beta
for k=1:ParNum
for i=1:NumPoints
    f(k)=power(x(i),k-1);
    %fprintf('   i=%d  f(%d)=%g \t',i,k,f(k));
    beta_element(k,i)=y(i)*f(k)/(ery(i)*ery(i));
    %fprintf('y(i=%d)=%g ery(i=%d)=%g \n',i,y(i),i,ery(i));
    %fprintf('beta(k=%d,i=%d)=%g \n',k,i,beta_element(k,i));
    beta(k)=sum(beta_element(k,:));
    %fprintf('beta_element(%d,%d)=%g
    %beta(%d)=%g\n',k,i,beta_element(k,i),k,beta(k));
end
end
%beta

% finding matrix alpha
for k=1:ParNum
for l=1:ParNum
    for i=1:NumPoints
        f(k)=power(x(i),k-1);
        f(l)=power(x(i),l-1);
        alpha_element(k,l,i)=f(k)*f(l)/(ery(i)*ery(i));
        alpha(k,l)=sum(alpha_element(k,l,:));
        %fprintf('alpha_element(%d,%d,%d)=%g alpha(%d,%d)=%g\n',k,l,i,
        alpha_element(k,l,i),k,l,alpha(k,l));
    end
end
```

```
end

%alpha

%To find fit parameters, need to invert matrix alpha.

alpha_invert = inv(alpha);

%alpha_invert

% The fit is y = a(1) + a(2)*x + a(3)*x*x

%fit parameters by matrix inversion method

parameter = beta*alpha_invert; %a(1)=parameter(1)

%parameters

fit_m_inver = parameter(1) + parameter(2)*x + parameter(3)*x.*x;

% error on the parameters

er_a = sqrt(diag(alpha_invert));

%fit parameters by MatLab

par = polyfit(x,y,2);

%par

fit_MatLab = par(3) + par(2)*x + par(1)*x.*x;

%Get Emittance and Twiss parameters from fit

gamma = En/me;

er_gamma = En_er/me;

beta = sqrt(1-1/gamma^2);

er_beta = er_gamma/(gamma^3*beta);

A=parameter(3);

B=-parameter(2)/(2*A);
```

```
C=parameter(1)-A*B^2;
erA = er_a(3);
erB = sqrt( (-er_a(2)/(2*A))^2 + (parameter(2)*erA/(2*A^2))^2 );
erC = sqrt((er_a(1))^2 + (-B^2*erA)^2 + (-2*A*B*erB)^2);
%fprintf('A=%g+-%g  B=%g+-%g  C=%g+-%g\n',A,erA,B,erB,C,erC);

emit = sqrt(A*C)/((S12)^2);
er_emit = sqrt( (1/2*A^(-1/2)*A^(1/2)*erA/(S12)^2)^2 +
(1/2*A^(1/2)*A^(-1/2)*erC/(S12)^2)^2 + ( 2*sqrt(A*C)*erS12/(S12)^3)^2 );
emit_n = emit*gamma;
er_emit_n = sqrt((emit*er_gamma*beta)^2+(emit*gamma*er_beta)^2+
(er_emit*gamma*beta)^2);
beta_func = sqrt(A/C);
er_beta_func = sqrt( (1/2*sqrt(1/(A*C))*erA)^2 + (-1/2*sqrt(A/C^3)*erC)^2 );
alpha_func = beta_func*(B + 1/S12);%alpha_func = sqrt(A/C)*(B + 1/S12)
er_alpha_func = sqrt(((B+1/S12)*er_beta_func)^2 + (beta_func*erB)^2 +
(-beta_func*erS12/(S12)^2)^2 );

figure(1)

set(axes,'FontSize',40)
pardat = errorbar(x,y,ery,'MarkerSize',30,'Marker','.','LineStyle','none',...
'LineWidth',3,...
'DisplayName','Data Points',...
'Color',[0 0 1]);
hold on

%Plot fit done by matrix inversion method.
```

```
parfit_m_inver = plot(x,fit_m_inver,'r');
set(parfit_m_inver,'LineWidth',3);

legend('Data','Fit');
set(legend,'Position',[0.73 0.75 0.1 0.1]);
set(legend,'FontSize',40);
set(legend,'FontName','Times New Roman');

hx = xlabel('k_{1}L (m^{-1})','FontSize',48,'FontName','Times New Roman');
hy = ylabel('\sigma^2_x (mm^2)','FontSize',48,'FontName','Times New Roman');
box off; % remove the top and right axes

%set(gca,'ticklength',4*get(gca,'ticklength'));
set(gca,'ticklength',[0.06 0.9]);
fit=title('');
%fit=title('15.6 MeV, X-Projection: k_{1}L vs \sigma^2');
set(fit,'FontSize',24,'FontWeight','bold','FontName','Times New Roman');
axis([-0.05 0.55 2.3 3.2]); %axis([xmin xmax ymin ymax])
%axis('FontSize',28);

saveas(fit,'Emit_Calc_plots\par_fit_x.fig','fig');
saveas(fit,'Emit_Calc_plots\par_fit_x.eps','epsc');
saveas(fit,'C:\Users\sadiq\Desktop\IPAC12\Paper\par_fit_x.eps','epsc');
saveas(fit,'Emit_Calc_plots\par_fit_x.png','png');
drawnow

fprintf('x-projection:\n\nemit=%.3f +- %.3f mm*mrad, emit_norm=%.2f +-
%.2f mm*mrad \n\n', emit, er_emit, emit_n, er_emit_n);
```

```
fprintf('beta=%.2f +- %.2f m, alpha=%.2f +- %.2f rad \n\n', beta_func,
er_beta_func, alpha_func, er_alpha_func);
fprintf('parabola fit for y-projection (y in mm unit): \n y = (%.5f +-%.5f)
+ (%.5f+-%.5f)*x + (%.5f+-%.5f)*x.*x \n\n', parameter(1),er_a(1),
parameter(2),er_a(2), parameter(3),er_a(3));
return
```

References

[1] S., Chemerisov. and C. D., Jonah, “Generation of high intensity thermal positron beams using a 20-MeV electron linac,” *INTERNATIONAL WORKSHOP ON POSITRONS AT JEFFERSON LAB*, Newport News, Virginia, 2009.

[2] North Carolina State University, *http://www.ne.ncsu.edu/nrp/ips.html*, Intense Positron Beam, Nuclear Reactor Program, 2013-06-28.

[3] M. N. Rosenbluth, *Phys. Rev.*, 18, 1014 (1950).

[4] R. C.Walker *et al.*, *Phys. Rev. D*, 49, 5671 (1994).

[5] J. Arrington, *Phys. Rev. C*, 68, 034325 (2003).

[6] R. C. Walker, *Ph.D. thesis*, California Institute of Technology, 1989.

[7] H.W. Koch & J.W Motz, *Rev. Mod. Phys.*, 31, 920 (1959).

[8] K. S. Krane, *Introductory Nuclear Physics*, John Wiley & Sons, New York, 1988.

[9] NIST, *http://physics.nist.gov/cgi-bin/Xcom/xcom2*, NIST XCOM, 2013-05-03.

[10] M. Conte, & W. W. Mackay, *An Introduction To The Physics Of Particle Accelerators*, World Scientific, New York, 2008.

[11] V.L Ginzburg & I.M. Frank, *Sov. Phys. JETP*, 16, 15 (1964).

[12] K.T. McDonald and D.P. Russell, Fron. of Par. Beams Obser. Diag. and Cor. **08544**, (1988).

[13] Y. Kim *et al.*, in *Proc. FEL*2008, Gyeongju, Korea.

[14] D.F.G. Benedetti, *et al.*, Tech. Rep., DAFNE Tech. Not., Frascati, Italy (2005).

[15] S.Y. Lee, *Accelerator Physics*, (Singapore: World Scientific, 2004), 61.

[16] F.J. Decker, NASA STI/Recon Tech. Rep. N **1994**.

[17] B. KC & Y. Kim, *http://www2.cose.isu.edu/-yjkim/course/2010fall/2010fall-ap-term-project06.pdf*, ISU Phys. Dept., 2013-05-26.

[18] SAINT-GOBIAN, *http://www.detectors.saint-gobain.com*, SAINT-GOBIAN CRYSTALS Technical Information Notes, 2013-06-11.